5-2024

Exploring the phase space of binary neutron star simulations and photon geodesics in the presence of black holes

Ben Fisler
bf1771@rit.edu

Exploring the phase space of binary neutron star simulations and photon geodesics in the presence of black holes

---

MS *Master of Science*

in Astrophysical Sciences and Technology

Ben Fisler

School of Physics and Astronomy

Rochester Institute of Technology

Rochester, New York

May 2024

ASTROPHYSICAL SCIENCES AND TECHNOLOGY

COLLEGE OF SCIENCE

ROCHESTER INSTITUTE OF TECHNOLOGY

ROCHESTER, NEW YORK

M.S. THESIS DEFENSE

Candidate: Ben Fisler

Thesis Title: Exploring the phase space of binary neutron star simulations and photon geodesics in the presence of black holes

Adviser: Dr. Joshua Faber

Date of defense: May, 2024

The candidate's M.S. Thesis has been reviewed by the undersigned. The Thesis

(a) is acceptable, as presented.

(b) is acceptable, subject to minor amendments.

(c) is not acceptable in its current form.

Written details of required amendments or improvements have been provided to the candidate.

Committee:

Dr. Yosef Zlochower, Committee Member

Dr. Jason Nordhaus, Committee Member

Dr. Joshua Faber, Thesis Advisor

Please submit form to AST Graduate Program Coordinator

ASTROPHYSICAL SCIENCES AND TECHNOLOGY
COLLEGE OF SCIENCE
ROCHESTER INSTITUTE OF TECHNOLOGY
ROCHESTER, NEW YORK

CERTIFICATE OF APPROVAL

M.S. DEGREE THESIS

The M.S. Degree Thesis of *Ben Fisler* has been examined and approved by the thesis committee as satisfactory for the thesis requirement for the M.S. degree in Astrophysical Sciences and Technology.

Dr. Yosef Zlochower, Committee Member

Dr. Jason Nordhaus, Committee Member

Dr. Joshua Faber, Thesis Advisor

Date

Exploring the phase space of binary neutron star simulations and photon geodesics in the presence of black holes

By

Ben Fisler

A dissertation submitted in partial fulfillment of the requirements for the degree of M.S. in Astrophysical Sciences and Technology, in the College of Science, Rochester Institute of Technology.

May, 2024

Approved by

Dr. Andrew Robinson	Date
Director, Astrophysical Sciences and Technology	

Abstract

Here, we investigate the use of the `Lorene` code to generate quasi-equilibrium initial data for close binary neutron star configurations. The code has been widely used throughout the field of numerical relativity, and is capable of generating initial data for a wide range of neutron star equations of state and binary mass ratios. We also explore the ranges of parameter space for which the code can generate accurate initial data, and the nature of the instabilities that arise when the code is asked to produce data outside this range. This work should aid other groups performing merger simulations of binary neutron star systems to select appropriate initial data with which to launch simulations.

We also report on a code for calculating photon geodesics moving within the curved space-time of a black hole. The ultimate goal of this work is to calculate approximations for the light deflection in terms of the initial parameters of the system. An error analysis is conducted for the code, and future work on the numerical approach is discussed.

Contents

List of Figures

List of Tables

Chapter 1

Introduction: BNS initial data and light bending

In this thesis we explore two problems in relativistic astrophysics, the generation of quasi-equilibrium initial data for binary neutron star systems, and the light deflection around Kerr black holes. We seek to develop and test the performance of numerical tools used within the field to simulate relativistic astrophysical phenomena of binary neutron stars and a photon traveling near a black hole.

For the first project on binary neutron star initial data, our work builds upon [3] which allows for the simulation of binary neutron stars with unequal mass ratios. This code was built off of the `Lorene` code, [2] which is a popular astrophysical code used to obtain a quasiequillibrium relativistic binary neutron star system [3]. Since the neutron star equation of state is unknown, one goal of these simulations is to produce initial data for mass and radius relationships of neutron stars by running code that approximates the neutron star equation of state and varies neutron star central density to produce models with different masses and radii. `Lorene` is used by many astrophysicists, but it often crashes or struggles to converge, and there is almost no documentation or mentions of the code breaking down and producing inaccurate results. This thesis also goes into some detail on initial data that causes `Lorene` to produce inaccurate results and some insights as to why these inaccuracies occur.

In the second project, we investigate the simulation of a photon curving around a black hole. Since it's nearly impossible to observe a photon's path curve around a black hole, we run simulations based on mathematical equations to observe this behavior. The goal of this project is to use the simplified equations for the path of a photon taken from [4], in hopes that it will be easier for less experienced scientists to understand our work and use our code. The equations for the path of a photon involve elliptic integrals which are computationally intensive due to the fact that they can only be evaluated numerically [5]. Approximating these equations in simpler forms is a popular technique with many examples such as [5] that uses an expansion series to approximate the equations for easier calculations. This thesis uses an approximation from [4] that discretizes the equations so they can be easily solved with an iterative process.

1.1 General Relativity

When studying neutron stars and black holes, it is not possible to accurately describe their properties using Newtonian physics alone due to the fact that they are both relativistic bodies. Both objects are massive enough that they curve spacetime around them, causing it to be very different from flat space. This curvature of space causes the event horizon of a black hole and lead to the TOV equation that describes the balance between a neutron star's gravity and pressure. Also, the large surface potentials of compact objects can only be accurately determined by general relativity due to their small size and extreme density [6].

Einstein developed the general theory of relativity to account for phenomena not properly captured in Newtonian physics, primarily the role of gravity on the underlying geometry of space. General relativity (GR) involves a four dimensional spacetime geometry, three dimensions for a curved space and one for time. The principle of GR states that uniformly accelerated motion and being at rest in a gravitational field are identical, indistinguishable for a freely-falling observer.

In practice, GR is a theory of gravitation that involves solving the field equations derived by Einstein for the metric tensor that defines the curvature of the spacetime and how objects

move within it. Einstein's field equations can be written as

$$R_{\mu\nu} - \frac{1}{2}Rg_{\mu\nu} + \Lambda g_{\mu\nu} = \kappa T_{\mu\nu} \tag{1.1.1}$$

Here, κ is the gravitational constant defined as $\frac{8\pi G}{c^4}$, Λ is the cosmological constant that seemingly contributes to the expansion of the universe, $g_{\mu\nu}$ is the metric tensor that captures all the geometry of spacetime, $R_{\mu\nu}$ is the Ricci curvature tensor that measures how a given spacetime differs from flat space, and R is the scalar curvature (the trace of the Ricci tensor) that depends on only the metric tensor and its first and second derivatives.

These equations and the resulting theory of GR incorporate effects such as spacetime curvature due to gravity, whose consequences are as wide-ranging as affecting the paths of photons through space, the production of gravitational radiation, and the expansion of the universe [7]. The trajectories of photons are described by the geodesic equations, while the gravitational field is described by the Einstein field equations. The field equations relate spacetime curvature to the local energy and momentum densities via the stress energy tensor, which describes the density and flux of energy and momentum in spacetime. In GR, gravity is not considered to be a traditional force like in Newtonian physics, but rather an effect of curved spacetime geometry, where the stress energy tensor causes the curvature. Note that according to GR, mass is not the only source of gravity; GR states that mass and energy are the same thing in a different form through the famous formula $E = mc^2$. Thus, all sources of energy gravitate, including but not limited to (baryonic) mass-energy. GR also predicts gravitational waves propagating via the curvature of spacetime when produced by massive objects, with the strongest amplitudes thought to be created by the mergers of black holes and neutron stars.

1.2 Compact objects

Our work here investigates the properties of neutron stars (NS) and black holes (BH). These are the most dense objects in the universe and are often modeled in simulations due to the fact

that they are very difficult to observe. Since NSs and BHs can produce gravitational waves during binary mergers, they are commonly studied in simulations to learn more about the objects involved in the mergers. Gravitational waves are a huge topic in modern astrophysics due to the fact that they confirm general relativity and the detectors have only been around for a few years. The next section introduces essential information on compact objects, starting with an introduction to NSs, their unknown equation of state, and the formation of binary NS systems. Then the thesis goes into an introduction on BHs and how their gravity can affect the paths of photons around them.

1.2.1 Neutron Stars

NSs are the dead remnants of a star with an initial mass of approximately 8 to 25 solar masses, formed at the end of the star's life during the supernova process. When a star of this mass range undergoes gravitational collapse, gravity is able to compress the star further than electron degeneracy pressure can counteract (which would yield a white dwarf), causing the electrons and protons in the atoms to combine into neutrons, creating a NS. NSs are not supported by gas and radiation pressure like normal stars, but by nuclear forces. Nuclear forces start to saturate as the nucleons begin to touch at high densities ($\sim 10^{15}\mathrm{g/cm}^3$). The force is attractive for a small number of nucleons, but becomes repulsive for a larger number [6].

NSs, particularly ones accreting matter from a companion, can spin up to periods as short as a few ms [8]. Some of these rapidly rotating NSs emit electromagnetic radiation due to their magnetic fields and extreme spin. This happens, primarily in the radio regime, by the acceleration of charged particles along the magnetic field lines of highly magnetized rotating NSs [1], causing charged particles to accelerate, and this is magnified near the poles where the magnetic field is strongest. These are called pulsars, and the best theoretical models predict that they constantly emit light in the general direction of their poles, observed at periodic times depending on one's line of sight.

NSs are the densest known objects in the universe other than BHs, but they are quite small

in size, typically only 10 to 15 km in radius [9]. They are initially very hot with temperatures greatly exceeding 10^{10} Kelvin [10] but lack the chemical composition to sustain nuclear fusion, so over time they cool due to emission processes, including energy losses to both neutrinos and photons [10]. Isolated NSs are typically quite difficult to observe, since their luminosity is very small given their size ($L = 4\pi r^2 \sigma T^4$), unless one happens to be a pulsar with one pole facing earth. Surprisingly, a few isolated NSs have been found, including serendipitous discoveries such as RX J185635-3754 [11].

A fraction of NSs are in binary systems with another NS, but in many cases it is difficult to measure precisely all of the properties of both NSs as well as those of the orbits themselves. A binary NS system can give off x-rays during accretion, but many X-ray binaries have faint optical emission or are located near the galactic center, making observations difficult [12]. Another uncertainty is the mass distribution [13], since NSs that have evolved differently show distinctive properties through dissimilar distribution peaks and mass cutoff values. Additionally, the lower bound on the NS mass is not well known because it is determined by the unknown equation of state (see below). All of these uncertainties allow for poor constraints on the mass distribution of NSs. More uncertainty also comes from the fact that measures of NS masses are typically indirect or rely on chains of inference [14]. NS mass distributions are currently a significant topic of research due to the their uncertain nature and difficulties in detection.

1.2.2 TOV equation: derivation and solutions

The Tolman-Oppenheimer-Volkoff (TOV) equation is a differential equation that describes the structure of a spherically symmetric, non-rotating star in general relativity. It may be derived from the Einstein field equations for a perfect fluid and models the interior of a NS.

The derivation [15], typically starts with a symmetric vacuum spacetime outside of a star in spherical coordinates.

$$g_{\mu\nu} = \begin{pmatrix} -(1-\frac{2GM}{rc^2})c^2 & 0 & 0 & 0 \\ 0 & (1-\frac{2GM}{rc^2})^{-1} & 0 & 0 \\ 0 & 0 & r^2 & 0 \\ 0 & 0 & 0 & r^2\sin(\theta)^2 \end{pmatrix} \tag{1.2.2}$$

which is equivalent to the following line element

$$ds^2 = g_{\mu\nu}dx^\mu dx^\nu = -\left(1-\frac{2GM}{rc^2}\right)c^2dt^2 + \left(1-\frac{2GM}{rc^2}\right)^{-1}dr^2 + r^2(d\theta^2+\sin^2\theta d\phi^2) \tag{1.2.3}$$

Following the standard conventions of the relativity community, we will assume for the remainder of this thesis that units are chosen such that $c = 1$, unless otherwise specified. Under that choice, the line element of a spherically symmetric object takes the form

$$ds^2 = g_{\mu\nu}dx^\mu dx^\nu = -\left(1-\frac{2GM}{r}\right)dt^2 + \left(1-\frac{2GM}{r}\right)^{-1}dr^2 + r^2(d\theta^2+\sin^2\theta d\phi^2) \tag{1.2.4}$$

Covariant derivatives in general relativity, indicated by ∇, are calculated by defining the Christoffel symbols Γ as a way to connect different points in spacetime. When applied to a tensor with one contravariant and one covariant index, for instance, we have as a generalization of a partial derivative that

$$\nabla_\mu T^\alpha_\beta = \partial_u T^\alpha_\beta + \Gamma^\alpha_{\sigma\mu}T^\sigma_\beta - \Gamma^\sigma_{\mu\beta}T^\alpha_\sigma \tag{1.2.5}$$

$$\Gamma^\mu_{\alpha\beta} = \frac{1}{2}g^{\mu\nu}\left[g_{\alpha\nu,\beta} + g_{\beta\nu,\alpha} - g_{\alpha\beta,\nu}\right]. \tag{1.2.6}$$

In this case, the comma denotes differentiation with respect to the coordinate x^μ so that $f_\mu = \frac{\partial f}{\partial x^\mu}$. The Christoffel symbols are used to construct the Ricci tensor

$$R_{\mu\nu} = \Gamma^\alpha_{\mu\nu,\alpha} - \Gamma^\alpha_{\mu\alpha,\nu} + \Gamma^\alpha_{\beta\alpha}\Gamma^\beta_{\mu\nu} - \Gamma^\alpha_{\beta\alpha}\Gamma^\beta_{\alpha\nu}, \tag{1.2.7}$$

which serves as a measure of the curvature of spacetime.

Assuming a static, spherically symmetric perfect fluid configuration for our NS, the resulting line element is then

$$ds^2 = \exp\left(-2\Phi(r)\right) dt^2 + \left(1 - \frac{2m(r)}{r}\right)^{-1} dr^2 + r^2\left(d\theta^2 + \sin^2\theta d\phi^2\right) \tag{1.2.8}$$

Now consider a perfect fluid with total energy density e, isotropic pressure P, and four-velocity $u^\mu = \left\langle \frac{dt}{d\tau}, \frac{dr}{d\tau}, \frac{d\theta}{d\tau}, \frac{d\phi}{d\tau} \right\rangle$. The stress energy tensor would then be equal to

$$T^{\mu\nu} = (e + P)u^\mu u^\nu + Pg^{\mu\nu} \tag{1.2.9}$$

The total energy density, e, consists of both the rest mass density of the fluid, ρ, and the internal energy, $\rho\epsilon$, where ϵ is the specific internal energy density, which in this case represents the thermal motion of the constituent fluid particles, and is given by $e = \rho(1+\epsilon)$. For simplicity we may drop the factors of c, knowing we may recover them if needed based on dimensional analysis. Finally, we define the specific enthalpy, h, or enthalpy per unit mass, as

$$h = \frac{e + P}{\rho}. \tag{1.2.10}$$

The derivation of the TOV equation can begin with the nonzero Christoffel symbols. In what follows, primes indicate radial derivatives, i.e., $m' \equiv \frac{dm(r)}{dr}$.

$$\Gamma^t_{tr} = \Phi' \tag{1.2.11}$$

$$\Gamma^r_{tt} = = \Phi' \exp(2\Phi)\left(1 - \frac{2m}{r}\right) \tag{1.2.12}$$

$$\Gamma^r_{rr} = \frac{rm' - m}{r^2 - 2rm} \tag{1.2.13}$$

$$\Gamma^\theta_{r\theta} = \Gamma^\phi_{r\phi} = \frac{1}{r} \tag{1.2.14}$$

$$\Gamma^r_{\theta\theta} = \csc^2\theta\Gamma^r_{\phi\phi} = 2m - r \tag{1.2.15}$$

$$\Gamma^\theta_{\phi\phi} = -\csc^2\theta \tag{1.2.16}$$

$$\Gamma^\phi_{\theta\phi} = -\sin(\theta)\cos(\theta) \tag{1.2.17}$$

From Equation (1.2.7), the independent non-zero components of the Ricci tensor are

$$R_{tt} = \exp(2\Phi)(\Phi'' + \Phi'^2)\left(1 - \frac{2m}{r}\right) + \Phi'\left(\frac{2r - 3m - rm'}{r^2}\right) \quad (1.2.18)$$

$$R_{rr} = \left(1 - \frac{2m}{r}^{-1}\right)\left(\frac{(rm' - m)(2 + r\Phi')}{r^3}\right) - \Phi'' - [\Phi']^2 \quad (1.2.19)$$

$$R_{\theta\theta} = csc(\theta)^2 R_{\phi\phi} = (2m - r)\Phi' + m' + \frac{m}{r} \quad (1.2.20)$$

Therefore the Ricci scalar is

$$R = g^{\mu\nu}R_{\mu\nu} = 2\left[\frac{2m'}{r^2} + \frac{2m'}{r^2} + \Phi'(3m - 2r + rm') - \left(1 - \frac{2m}{r}\right)(\Phi'' + \Phi'^2)\right] \quad (1.2.21)$$

If one ignores the cosmological constant term (which is irrelevant for our work here on compact objects), the Einstein equations take the form

$$G_{\mu\nu} = R_{\mu\nu} - \frac{g_{\mu\nu}R}{2} = 8\pi T_{\mu\nu} \quad (1.2.22)$$

where in the Eulerian rest frame,

$$T_{tt} = \exp(2\Phi)e \quad (1.2.23)$$

so the 'time-time' component of the equation gives

$$G_{tt} = \frac{2m'\exp(2\Phi)}{r^2} = 8\pi\exp(2\Phi)e \quad (1.2.24)$$

or, equivalently,

$$\frac{dm}{dr} = 4\pi r^2 e \quad (1.2.25)$$

For the radial component of Einstein's equations, we have

$$T_{rr} = \left(1-\frac{2m}{r}\right)^{-1} P \tag{1.2.26}$$

$$G_{rr} = \frac{2}{r}\left(\Phi' - \frac{m}{1-2m/r}\right) = \frac{8\pi P}{1-2m/r} \tag{1.2.27}$$

$$\frac{d\phi}{dr} = \frac{m+4\pi r^3 P}{r(r-2m)} \tag{1.2.28}$$

Finally, we need a differential equation for the pressure. The most straightforward way to derive this is to use conservation of energy to argue that the divergence of the stress-energy tensor vanishes. The radial component is sufficient in what follows. If

$$T^{\mu\nu} = diag\left(\exp(-2\Phi)e, \left(1-\frac{2m}{r}\right)P, r^{-2}P, r^{-2}\csc^2\theta P\right) \tag{1.2.29}$$

then we have

$$0 = \nabla_\nu T^{r\nu} = \frac{\partial T^{r\nu}}{\partial x^\nu} + T^{\sigma\nu}\Gamma^r_{\sigma\nu} + T^{r\sigma}\Gamma^\nu_{\sigma\nu} \tag{1.2.30}$$

$$= \frac{\partial T^{rr}}{\partial r} + T^{tt}\Gamma^r_{tt} + T^{\theta\theta}\Gamma^r_{\theta\theta} + T^{\phi\phi}\Gamma r\phi\phi + T^{rr}\Gamma^\nu_{r\nu} \tag{1.2.31}$$

$$= \left(1-\frac{2m}{r}\right)(P' + (P+e)\Phi') \tag{1.2.32}$$

and thus $\frac{dP}{dr} = -(e+P)\frac{d\Phi}{dr}$. The TOV equations may be summarized as

$$\frac{dm}{dr} = 4\pi r^2 e \tag{1.2.33}$$

$$\frac{dP}{dr} = -(e+P)\frac{m+4\pi r^3 P}{r(r-2m)} \tag{1.2.34}$$

$$\frac{d\Phi}{dr} = -\frac{1}{e+P}\frac{dP}{dr} \tag{1.2.35}$$

These equations may be closed by specifying an equation of state (EOS) linking how e and P depend on the density ρ. We note, though, that the definition of the quantity ρ is used inconsistently throughout the NS literature. Derivations of the TOV equation typically as-

sume that ρ is the gravitational energy density, including both baryonic and internal energy contributions, whereas in the relativity community, it typically refers to only the baryonic mass density contribution. Here, we adopt this latter convention throughout. This does have practical consequences at times, as for polytropic EOS, discussed below, one must specify *which density applies* if the pressure is given as a power-law in terms of the density ρ.

1.2.3 Neutron star equation of state

Very little is known in detail about the EOS of NS matter, given the difficulties in experimentally reproducing the extremely large densities present in their interiors ($\sim 10^{15}\mathrm{g/cm}^3$). In principle, the EOS can be inferred from observations, particularly those of NS masses and radii, but in practice it is difficult to determine both of these simultaneously [16]. At present, this remains perhaps the greatest uncertainty in the physics of NSs, and represents one of the most interesting theoretical and observational challenges astronomers studying these systems face.

NS EOS models are typically described as being "soft" or "stiff"; soft equations of state produce smaller changes in pressure for a given change in density and stiff equations of state much larger changes. Unsurprisingly, soft equations of state are much easier to compress due to their smaller pressure changes. Not only are there observational constraints on mass and radius, but there are constraints on soft and stiff equations of state. One immediate constraint on EOS models is related to causality, $dP/d\rho = c_s^2 \leq 1$, which demands the sound velocity c_s to be smaller than the speed of light. In practice, softer low-density equations of state cannot be easily combined with stiff high-density ones, because $dP/d\rho$ grows more rapidly than would be physically reasonable, resulting in pressure-density curves with nearly infinite slopes. The low and high density equations of state effectively constrain each other [16].

The saturation density is the point where adding more nucleons does not significantly increase the binding energy per nucleon or the overall density. For individual nuclei, the saturation density is close to the density of heavy nuclei. Since they are so close, laboratory experiments can infer the properties of nuclear matter for nuclei. The problem with NSs is

they are so much larger than heavy nuclei that we can not make the same assumptions about their properties like we can with heavy nuclei in lab experiments. The increase in size from a single nucleus to a NS creates more uncertainties and complications that can drastically change the radius of the NSs by a matter of kilometers. Since the pressure of nuclear matter is so large, even minor corrections from various particle interactions will change the predicted properties of NSs dramatically [16].

Due to its complexity, the NS EOS is often modeled as a polytrope of the form $P = \kappa\rho^{\gamma}$. Here κ is a constant that can be approximated based on the desired properties of the NS mass-radius relation, and γ is the adiabatic index that determines how the pressure scales with density. Fixing the central enthalpy and adiabatic index, and increasing the overall pressure scale creates a variety of NSs with increasing mass and radius for a given compactness $C \equiv \frac{GM}{Rc^2}$ [9]. This method is often used in simulations to create sequences of NS models because it allows for a quick production of a range of models with varying physical parameters.

1.2.4 Binary neutron star: formation and mergers

Figure 1.1 shows different outcomes for a binary star system where each star has the potential to become a NS. Recycled pulsars are out of the scope of this thesis, but they occur when a pulsar's rotation begins to speed up again due to accretion [8].

Stars are often found in binary systems, and NSs are no exception. When both stars in the system are massive enough, around 8-25 solar masses, we expect both to produce a Type Ib, Ic, or II supernova eventually. In these cases, the more massive star evolves faster and will eventually leave behind what will become the heavier compact object [17]. This may cause the system to unbind, depending on the mass loss from the system and the kick imparted to the primary during the explosion. If it does not, then the system will remain a binary, with one NS component orbiting either a main sequence or post-main sequence companion. The strong gravity of the NS may cause some mass transfer from the other star once the secondary expands during the post-main sequence giant phases. This mass transfer is important because the accretion onto the NS occurs over a long period of time, which allows it to generate energy

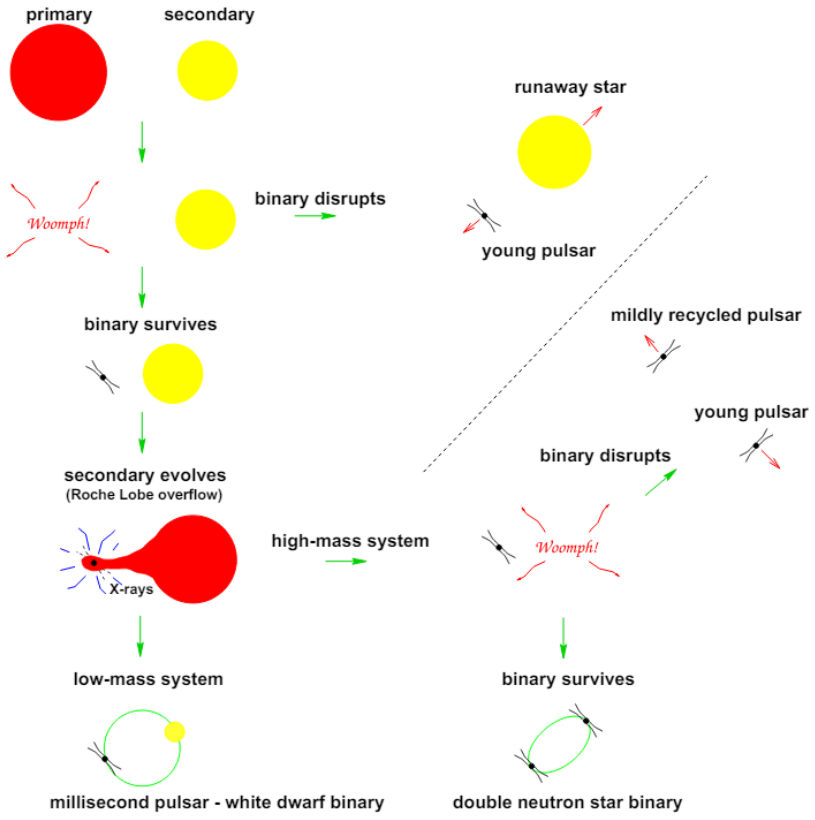

Figure 1.1: Binary NS formation. This thesis focuses on the route that starts as a primary and secondary star, then goes down the path to Roche Lobe overflow, then to a high-mass system and ends as a double NS binary [1].

and emit x-ray emission, while also stripping the other star of material [18]; such systems are known as high-mass x-ray binaries (HMXBs). This x-ray emission makes it easier to detect and learn more about the life cycle of a binary system that ends as two NSs. For systems that are sufficiently close, according to population synthesis calculations for merging NS-NS, the first-born compact object goes through a common-envelope with the second star [17]. This causes dynamical friction to reduce the orbital separation by several orders of magnitude. The large energy release due to friction and accretion during this spiral-in process is expected to cause the hydrogen-rich envelope of the giant to be expelled such that a very close binary remains, consisting of the helium core of the giant together with the neutron star [19]. Depending on the separation distance from the NS, mass transfer can still occur in this phase [18]. If the helium star still has sufficient mass, it will eventually explode as a supernova, and then second NS in the system is born; the secondary will be a NS without a history of accretion and is therefore expected to resemble the "normal" strong magnetic field single radio pulsars [19]. Binary NS systems are somewhat rare in nature but are of interest to astronomers due to the fact that they can produce gravitational waves.

Gravitational waves are produced when massive objects accelerate, and are strongest for high-density objects moving at relativistic speeds in relativistic gravitational potentials. The first time gravitational waves were detected happened in 2015, when a signal was seen by the two detectors from LIGO, in Hanford, WA and Livingston, LA. GW150914 was a BH binary system, at a distance of approximately 410Mpc from earth. The gravitational waves were produced by the merger of this system, with initial masses of 36 solar masses and 29 solar masses, respectively. LIGO detected the signals over a frequency range spanning 35 - 250 Hz, and at a strain amplitude of

$$h_s \approx 1.0 \times 10^{-21}$$

over interferometric detector arms of length L$\approx 4 \times 10^3$m [20]. This detection of gravitational waves is more evidence for GR because it directly involves the curvature of spacetime, in accordance with the predictions of the Einstein field equations. Over the past decade, LIGO

has now detected 90 sources [21]. The detection of gravitational waves is now well underway and will continue to be a large area of research in the future.

When a binary system of NS is formed, they will begin to spiral inward due to their extreme gravity. Eventually, they will form either a much more massive NS, or much more likely, a BH. During the inspiral, they will release gravitational waves because they are losing orbital energy.

1.3 Black holes

BHs are the densest known objects in the universe and originate from stars with masses of approximately $25M_{\odot}$ or more. When these stars collapse, they have enough mass to compress them further than the nuclear pressure that a NS could support, creating a BH. NSs that are too compact or accrete matter from a companion can even collapse into BHs as well. They are a singularity whose event horizon is outside of its own radius, causing any object that crosses the event horizon to be trapped inside the BH forever [6].

Like NSs, BHs can also be found in binary systems with other BHs or even NSs. These binary systems are inspiring the next generation of gravitational wave detectors due to the fact that their mergers produce gravitational waves. Many complex simulations and codes have been created to model the mergers of BHs and or NSs, as well as the interactions of these compact objects.

BHs that accrete matter often have a spin associated with them due to the angular momentum of the accretion disk. If an object is moving in the direction of the BH's spin, it will have a prograde orbit and curve towards the black hole. If the object is moving in the opposite direction of the spin, it will have a retrograde orbit and slightly curve away due to the fact that the BH's spin and gravity are trying to change the direction of the object. This affect is called frame dragging and can lead to a large and fast spinning accretion disk [6].

In addition to gravitation fields, both electric and magnetic fields exist intrinsically from BHs. Although one might not expect that astrophysical BHs have a large residue electric charge, some accretion scenarios were proposed to investigate the possibility of spin-

ning charged BHs. Moreover, theoretical considerations, together with recent observations of structures near Sgr A*, indicate possible presence of a small electric charge of the central supermassive BH [4]. The spin and charge of a BH can be used to define different types of BHs mathematically. A BH with spin and no charge is a Kerr BH and a BH with spin and charge is a Kerr-Newman BH. The Kerr metric and Kerr-Newman metric are

$$ds^2 = -\left(1 - \frac{2Mr}{\Sigma}\right) dt^2 - \frac{4aMr}{\Sigma} \sin(\theta)^2 dt d\phi$$
$$+\frac{(r^2+a^2)^2 - a^2\Delta \sin(\theta)^2}{\Sigma} \sin(\theta)^2 d\phi^2 + \frac{\Sigma}{\Delta} dr^2 + \Sigma d\theta^2 [22] \tag{1.3.36}$$

$$ds^2 = -\frac{\Delta}{\Sigma}(dt - a\sin(\theta)^2 d\phi)^2 + \frac{\sin(\theta)^2}{\Sigma}\left[(r^2+a^2)d\phi - adt\right]^2 + \frac{\Sigma}{\Delta} dr^2 + \Sigma d\theta^2 [4] \tag{1.3.37}$$

where $\Sigma = r^2 + a^2\cos^2\theta$ and $\Delta = r^2 - 2Mr + a^2 + Q^2$. Here Q is charge and a is spin. Note that $Q = 0$ for Kerr BHs.

1.4 Geodesic equations for photons

Geodesics are essentially straight lines as they exist on a curved surface. Photons follow null geodesics: null because their spacetime interval is zero and they have no proper time. The events located inside the light-cone are time-like with respect to A and can be causally related. The events located outside the light-cone are space-like with respect to A, and hence causally disconnected from it because they could not travel to A in time to be causally related [23]. Fig 1.2 shows this boundary between space-like and time-like. Einstein's theory of General Relativity predicted the curvature of a photon's path in the presence of gravitating matter, and years later it was able to be demonstrated through a variety of experiments. Any massive object will curve spacetime around it so much that a photon travelling near that object will follow a curved geodesic, though the effect is most significant for compact objects

with relativistic gravitational potentials, particularly NSs and BHs. This has, e.g., allowed astronomers to see lensed bright sources behind galaxies because the galaxy's gravitation bent the path of the photon emitted from the bright source.

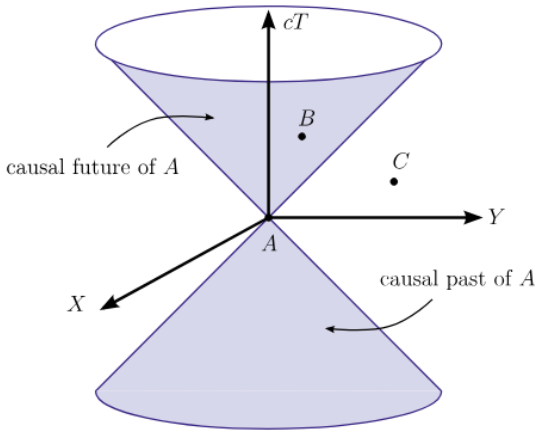

Figure 1.2: Light cone relative to A. Here time is the vertical axis and two dimensions of space are represented by the horizontal plane. Event B is in the causal future of A while event C is causally disconnected from A since it is outside of A's light-cone [23].

BHs have such strong gravity that if a photon is travelling tangentially to a BH, geodesics can bend by large angles around the BH before photons escape to infinity. If a photon is travelling in the right direction and sufficiently close, it can even fall into the BH, or spin around it forever and never escape because its gravity is so strong. The orbits of photons are affected by the spin of the BH and whether they are traveling in a prograde or retrograde direction with respect to it. Because of so-called "frame dragging" or gravito-magentism effects, prograde orbits are typically more stable against infall than retrograde ones.

Chapter 2

Numerical Techniques

All of the work in this thesis is based on numerical codes used to study binary NS systems and BH geodesics, respectively.

For binary NS systems, there is a multi-step process required to generate quasi-equilibrium binary configurations. We begin with the simplest step: generating equilibrium *isolated* NS models describing spherically symmetric, non-rotating NSs. This is done by approximating the equation of state by running the TOV code. The values from the TOV code will then be used to initialize the binary system by creating both stars and placing them in spacetime at their respective coordinates. The initial system will be read by the main code, Lorene, to relax the binary system towards equilibrium at fixed separations and then moves the stars inward.

2.1 Single NS parameter space

Given the uncertainties in the true physics of NS EOS, we must approximate it in all cases; often in the field, one approximates the pressure-density relationship as a power law to parameterize this uncertainty. One benefit of this approach is that it does allow one to use dimensional arguments to scale either the NS mass and radius, or alternately the parameters of the EOS model itself, to generalize from one model to similar ones.

To generate the physical parameters describing isolated NSs that will then be placed in a binary configuration, we use a code that approximates a solution to the TOV equations,

Eqs. (1.2.33),(1.2.34), (1.2.35), which allows us to specify the value of γ in the polytropic EOS $P = \kappa\rho^\gamma$, as well as the NS mass and radius (and thus the dimensionless compactness $\mathcal{C} \equiv GM/(Rc^2)$. The code first estimates the proper central enthalpy value and density, and uses this to generate a model whose total mass and radius are measured and whose compactness is then compared to the desired value. The surface is where the density goes to zero, and we linearly extrapolate in the proper power of the density ($\rho^{\gamma-1}$) to measure this location to high accuracy. Based on dimensional arguments, the TOV equation at the surface implies for a polytrope that

$$\frac{dP}{dr} \propto \frac{d}{dr}\rho^\gamma \propto \rho \quad \Rightarrow \quad \frac{d}{dr}\rho^{\gamma-1} \propto \text{const.}$$

The code then uses the shooting method to revise the central enthalpy to produce the desired compactness. If the compactness is too high based on the error threshold, then it will lower the pressure at fixed desnity via the parameter κ, and if the compactness is too low, it will increase it. This iteration typically converges quickly to the desired compactness. Once this is found, parameters may be rescaled so that all dimensionless quantities, particularly $P/(\rho c^2)$ and $GM/(Rc^2)$ remain fixed, but the mass and radius both take on their appropriate values.

This method also allows us to input artificially high radii or artificially small masses into the TOV code, for use in the Lorene code, which is typically more stable at the start of a quasi-equilibrium convergence calculation for lower-compactness systems.

2.1.1 TOV models for polytropes

For a given value of γ, polytropic NS models form a 1-parameter sequence, either in terms of the central enthalpy or the compactness, whose configurations may be rescaled to reproduce the desired physical values.

Indeed, for a configuration with a given compactness, one may produce a rescaling of the

mass and radius such that

$$M \to \alpha M; \quad R \to \alpha R \tag{2.1.1}$$

by modifying the equation of state and central density such that

$$\rho \to \quad \alpha^{-2}\rho; \quad \kappa \to \alpha^{2\gamma-2}\kappa \tag{2.1.2}$$

which has the effect of modifying the pressure $P \to \alpha^{-2}P$ while leaving the dimensionless quantities $GM/(Rc^2)$ and $P/(\rho c^2)$ invariant at a given reference location.

Based on these considerations, we choose as our reference model a NS configuration with a gravitational mass of $1.4M_\odot$ and a radius of 14km, and thus a compactness of $\mathcal{C} = 0.148$.

We can then vary the central density for each model while holding κ fixed to produce a mass-radius relation for the given EOS. Note that while configurations with extremely high central densities may be reached, NS models are known to be unstable to radial oscillations once the maximum mass is reached, and thus all models past that point are unphysical [6]. The maximum mass contains the last stable model for a NS [24]. Next, we use the `Lorene` code to generate binaries.

2.2 The Lorene code

The `Lorene` code is a free, publicly available set of routines in C++ that solve partial differential equations through multi-domain spectral methods, designed in particular to calculate quasi-equilibrium fluid configurations for NSs in binaries and the metric tensor of spacetime in general for both NS and BH systems [2]. Spectral methods involve representing functions as a sum of basis functions, typically built upon an orthogonal expansion. This has the advantage of high accuracy combined with efficiency, but includes the drawback that spectral methods cannot deal with sharp edges or discontinuities very well because of Gibbs' phenomenon [25]. Since the equations involve fluid configurations, and are therefore non-linear, discontinuities or other non-smooth behavior is unavoidable, especially at the surfaces of NSs as well as any

other locations in which the equation of state is not smooth with respect to the density. Discrete operators based on Taylor expansions, assuming smoothness of the solution, are going to fail near these regions and will produce less accurate solutions, often with artificial oscillations. [26]. To try to minimize this issue, Lorene breaks space into a set of nested radial domains, using a Chebyshev expansion in radius. In the center of each object, symmetry conditions are imposed to ensure that all allowed modes are smooth at the origin. The multidomain spectral method allows the physical discontinuity represented by the NS surface to be located at the boundary between the two innermost domains, so that all the fields considered are smooth in their respective domains and Gibbs phenomenon is minimized overall [27]. In the outermost domain, a coordinate transformation is used, $\xi = \frac{2R}{1-x}$, where R is the radius of the innermost boundary of the compactified external domain, to allow the entire exterior to be mapped to a finite range of the radial coordinate ξ [2]. The grid that Lorene uses consists of Chebyshev nodes in the radial direction such that the $\xi's$ of the grid are $N+1$ zeros of the Chebyshev polynomial of degree N + 1, an optimal choice known as a Chebyshev Gauss Grid [28]. For smooth solutions, this allows for spectral convergence, *exponential* decreases in overall error with respect to the number of modes employed, and even for non-smooth sources leads to very small numerical inaccuracies for reasonable numbers of coefficients. Because of the compactification, spatial infinity is the only location at which the code imposes exact boundary conditions (flat spacetime). In the angular directions for each domain, spherical harmonic expansions are implemented. This, along with Chebyshev polynomials in the radial direction, Legendre polynomials are used in the θ-direction and Fourier series are used in the ϕ-direction [2].

Overall, the method is extremely accurate. If the source terms for the elliptic equations to be solved decay as r^{-k}, the error of the numerical solution is shown to decrease at least as $N^{-2(k-2)}$, where N is the number of Chebyshev coefficients [27].

Here, we summarize the important concepts used in [2] to run quasiequilibrium relativistic binary NS simulations.

Before `Lorene` can simulate a binary NS system, it needs an initial system as input. This

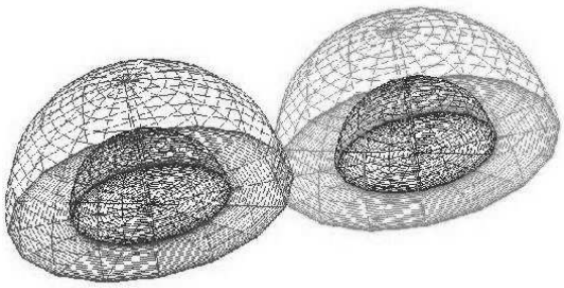

Figure 2.1: Lorene's grid is divided into sections. The innermost domain contains the NS which is then further divided into multiple shells. The outer domain seen in the figure starts at the surface of the NS and contains the non-compactified region of space just outside of the star. The last domain extends out to infinity and is not shown [2].

initial system consists of two NSs in spacetime. It requires the output of the TOV code, κ, γ and enthalpy, along with an initial separation distance and the number of domains in the θ, ϕ and radial directions. All of this information is then used to place the two NSs in spacetime with their equation of state, number of domains and the proper separation distance between them. At this time, the two stars have no effect on each other and have been simply placed near each other in spacetime. The main code of Lorene will then use this information from the initialization to create the binary system.

After the initialization, we relax the two NSs at equilibrium at a given separation using a relaxation factor multiplied by the enthalpy field and each auto-potential from the current and previous iteration [2]. Lorene also assumes the fluid is either rigidly rotating (corotating, tidally locked) or irrotational, and that the spatial 3-metric is conformally flat, i.e., flat up to a single overall scaling term known as the conformal factor. These assumptions allow for the elliptic equation of velocity potential to be solved and for the simulation of binary NSs.

2.3 Binary Neutron Star Evolution Codes

Many groups across the field have developed techniques to simulate binary NS systems. There are essentially two different parts to the problem. The first is to construct accurate binary NS initial data at a fixed moment in time, as opposed to dynamically evolving the gravitational

fields. This greatly simplifies the field equations [29]. Second, one must then dynamically evolve these initial data using the field equations for the spacetime metric and matter. Such calculations were first performed in full GR by Shibata and Uryu, who implemented a gamma-law EOS with $\gamma = 2$. This allowed them to evolve the equations of relativistic hydrodynamics, and Einstein's equations in what has become known as the BSSN formulation (Baumgarte-Shapiro-Shibata-Nakamura) [29].

One of the most widely used code within the numerical relativity community is the `Einstein Toolkit`, a collection of free, publicly available codes used for running relativistic astrophysical simulations, often involving magnetohydrodynamics. Although Lorene predates the Einstein toolkit, it can be used to initiate dynamical systems with the Einstein toolkit.

Lorene has a complex three dimensional mesh grid for high accuracy simulations. The number of domains inside and outside of the star is also set by the user to allow for a desired level of accuracy. The user can then set the number of points in each domain and in the theta and phi directions to increase or decrease resolution as needed. The three dimensional grid also decreases in resolution far away from the two stars. This is to save computation power for the simulation.

2.4 Techniques for calculating photon geodesics

For geodesics, we summarize the steps used in [4] to generate the coupled differential equations for the path of a photon. The null-like geodesic equation can be reduced from an elliptic integral to coupled differential equations. This is done by defining the four-velocity $u^\mu = \frac{dx^\mu}{d\sigma}$ in terms of an affine parameter, σ, since the metric of a Kerr Newman BH is independent of t and ϕ. This allows for the equations to be solved step by step instead of solving the computationally intensive elliptical equations for the entire path of the photon.

The simplified equations describing photon geodesics involve four coupled ordinary differential equations, for radius, θ, ϕ, and time, respectively, when expressed in spherical coordinates. For a Kerr-Newman BH of mass M, with dimensionless spin $a \equiv J/M^2$ and dimensionless charge Q, the equations are given for a photon of a given conserved energy E, azimuthal an-

gular momentum L, and Carter constant C (a relativistic generalization of the non-azimuthal angular momentum; see [4]) by:

$$\frac{dr}{d\sigma} = \sqrt{(r^2+a^2-a\lambda)^2-(r^2-2Mr+a^2+Q^2)(\eta+(\lambda-a)^2)} \tag{2.4.3}$$

$$\frac{d\theta}{d\sigma} = -\sqrt{\eta+a^2\cos(\theta)^2-\lambda^2\cot(\theta)^2} \tag{2.4.4}$$

$$\frac{d\phi}{d\sigma} = \frac{a}{(r^2-2Mr+a^2+Q^2)}(r^2+a^2-a\lambda)+\frac{\lambda}{\sin(\theta)^2}-a \tag{2.4.5}$$

$$\frac{dt}{d\sigma} = \frac{r^2+a^2}{(r^2-2Mr+a^2+Q^2)}(r^2+a^2-a\lambda)+a(\lambda-a\sin(\theta)^2) \tag{2.4.6}$$

where $\lambda = \frac{L}{E}$ and $\eta = \frac{C}{E^2}$. Here, σ is an affine parameter used to scale all four equations in the absence of a measure of proper distance for the photon's path. These equations allow for the evolution of a geodesic equation for light bending around a BH.

Our RK4 scheme advances all four equations simultaneously in Cartesian coordinates, and then stores the output for each variable in spherical coordinates to graph the photon's path. The Cartesian conversion was due to the fact that spherical equations violate the assumptions of uniqueness of solutions. This means that using spherical coordinates causes Eq. (2.4.3) to always equal zero, so the photon follows a circular path. The Cartesian conversions are shown below.

$$dx = dr\sin\theta\cos\phi + rd\theta\cos\theta\cos\phi - rd\phi\sin\theta\sin\phi \tag{2.4.7}$$

$$dy = dr\sin\theta\sin\phi + rd\theta\cos\theta\sin\phi + rd\phi\sin\theta\cos\phi \tag{2.4.8}$$

$$dz = dr\cos\theta - rd\theta\sin\theta \tag{2.4.9}$$

In these calculations, $r = \sqrt{x^2+y^2+z^2}$, $\theta = \arccos\frac{z}{r}$, and $\phi = \arctan\frac{y}{x}$. Setting r, θ and ϕ equal to spherical coordinates allowed us to convert from dr, $d\theta$ and $d\phi$ to dx, dy and dz while avoiding the issues of Eq. (2.4.3) at the first step. We did not alter $\frac{dt}{d\sigma}$ because it was not used in our calculations. Since it is nearly impossible to observe the correct path of a photon, we can not use observations to help confirm our code. Therefore, we implemented validation checks along the way to ensure the code is working properly. The first is setting the mass of

the BH equal to zero (this means there is no BH) and checking to see that the photon's path is a straight line. Next, as we're using RK4, halving the step size should yield results that are 16 times more accurate prior to numerical saturation. We continuously halved the step size to see if the error was 16 times smaller than the previous step.

Chapter 3

BNS Initial Data

We modified our TOV code so that it can modify the central density by varying factors (both larger and smaller) to output multiple NS models given initial reference mass and radius values. This allows us to consider a full sequence of models for a given EOS, up to and beyond the maximum mass marking the stability limit. In Fig. 3.1, we show gravitational mass vs. radius for different γ values. The compactness at each maximum gravitational mass for different γ values is shown in Fig. 3.2, while Fig. 3.3 shows the maximum compactness for different γ values. Fig 3.4 shows the baryonic mass vs. radius for different γ values.

It is clear to see from Figs. 3.1 and 3.4 that the gravitational mass is slightly smaller than the baryonic mass for our NS models. This is because the gravitational mass subtracts the binding energy from the baryonic mass [30]. This comes from the fact that energy is lost when particles are bound together.

In Fig. 3.2 We can then see the compactness where the gravitational mass is maximized. That is the true stability limit of the NS model. The compactness values here initially increase rapidly but start to level off as they approach the maximum compactness of any possible NS.

In Fig. 3.3 we can see that the maximum compactness for each γ value is very close to those in Fig. 3.2 where the compactness is calculated at the maximum gravitational mass. The reason they differ slightly, especially for lower γ values is because there are so many nonphysical models, these are models that mathematically exist but would not exist in nature. NSs with

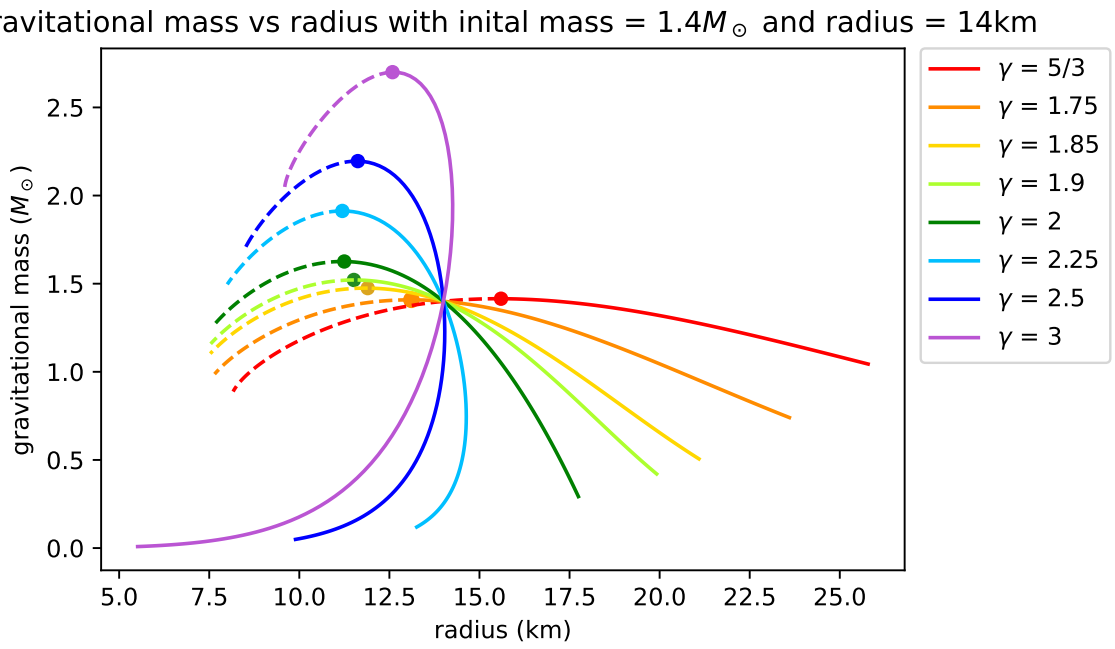

Figure 3.1: TOV gravitational mass and radius relationships for different γ values with initial data $1.4M_\odot$ and 14km radius. The dashed lines correspond to unstable models and the dot corresponds to the last stable model which contains the maximum gravitational mass for its γ value.

nearly zero mass are nonphysical because no massive star could lose that much mass and still be a NS. The low γ values have lower compactness values because they have a large decrease in radius while the mass hardly changes, while higher γ values have a decrease in both mass and radius, causing the larger difference in maximum compactness for smaller values of γ.

It's also worth noting that for $\gamma \lesssim 2.25$, we have an inverse relationship between mass and radius, which is true of Newtonian Lane-Emden solutions for $\gamma < 2$, with non-linear effects of relativistic gravitation accounting for the different cutoffs. For Newtonian models, values of γ greater than two lead to increasing mass for increasing radius, but in relativity, models with $\gamma = 2.25$ take on the role of having very little change in radius for widely varying masses at low mass, and every model considered has the inverse relationship at the highest masses.

For smaller γ values, those less than two, the radius changes considerably while the mass stays nearly constant. The opposite starts to happen when γ is greater than two, the radius hardly changes while the mass changes drastically. Interestingly, larger γ values can produce

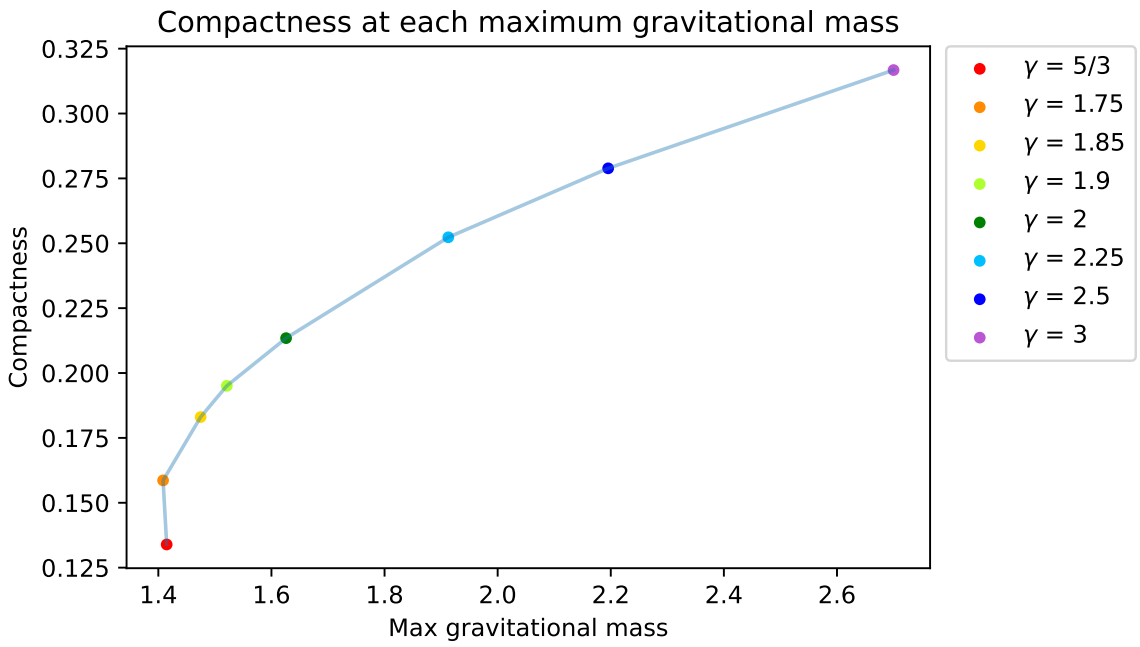

Figure 3.2: Compactness values at each maximum gravitational mass for Fig. 3.1 for different γ values.

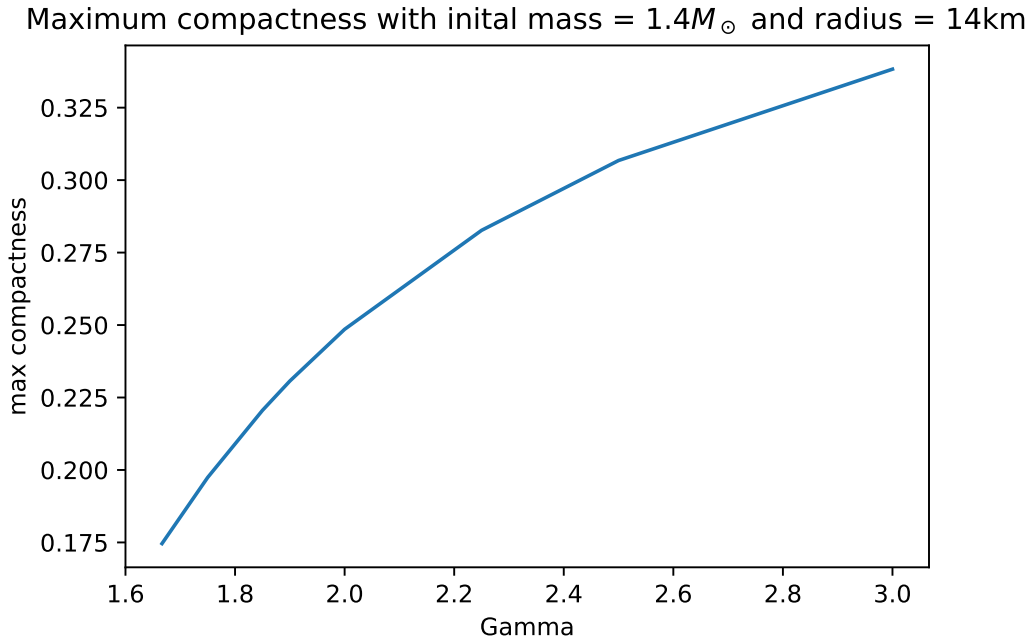

Figure 3.3: maximum compactness at each γ value for Fig. 3.1, including unstable models.

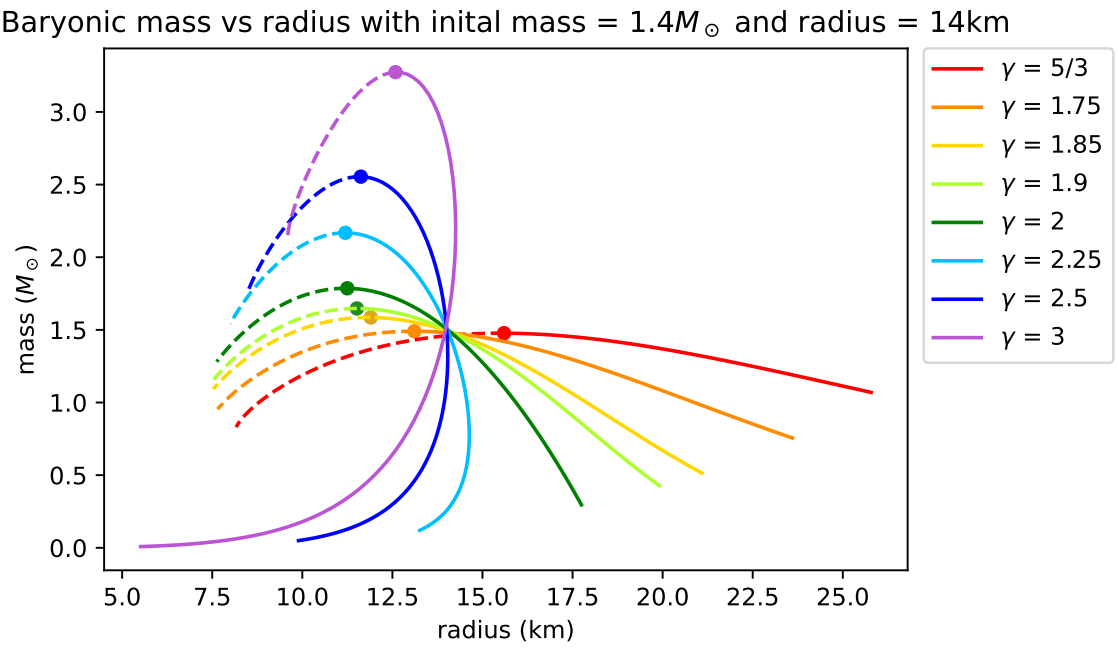

Figure 3.4: TOV baryonic mass and radius relationships for different γ values with initial data $1.4M_\odot$ and 14km radius. conventions are as in Fig. 3.1.

two different masses with different central densities for a single radius, although one of those (the dashed curve) is not a physical model, just a mathematical result of the solution to the simplified TOV equation. The maximum compactness graph shows that the maximum compactness increases monotonically, but with decreasing slope as γ increases, reaching the limit for the largest γ value considered.

3.1 BNS initial data via Lorene

3.1.1 Description of our routines, initial data generation and dynamical simulations of binary NS systems

Our working version of the `Lorene` code was developed by RIT AST PhD student Tanmayee Gupte working with Prof. Joshua Faber. Her work, [3], allowed Lorene to perform much more stably for simulations involving NSs with unequal mass ratios by fixing internal numerical root-finding routines that otherwise produce spurious errors, along with developing routines

to adjust NS masses and binary separations so that models are initially relaxed at lower masses and larger separations, the most stable region of parameter space for the code, and then slowly evolved to the desired final configuration in as stable a manner as possible.

Generating binary configurations in `Lorene` involves two different routines. The first part of the code computes solutions to the TOV equation, based on a specified EOS and central enthalpy for each star. A built-in TOV code generates a model for the structure of each NS, assuming spherical symmetry (and no rotation). Users may specify the pressure-density relation in a number of ways, with options including using power-laws (polytropes), piecewise polytropes, or tabulated models.

In this work, we focus on polytropes. To determine the correct central enthalpies corresponding to a NS of a given mass, radius, and EOS, we use our own TOV code implementation to determine the appropriate values to pass to `Lorene`. For tabulated and piecewise equations of state, neither of which typically have any free parameters to choose to describe the pressure-density relationship, one can change the central density and seek out a desired mass or radius but not both. For polytropes with a given adiabatic index γ, one is free to choose the polytropic constant κ to yield a desired mass and radius, found by searching for the central enthalpy that reproduces such a configuration (or, equivalently, central density given the monotonic dependence of one on the other). Our TOV code computes all the values needed for `Lorene`'s initial run, which, along with a set of grid-sizes and other `Lorene`-specific relaxation and convergence parameters, allow for the initial `Lorene` step to be performed. With these details specified, `Lorene` first generates two isolated TOV configurations, and places them in a binary system *without solving for any terms involving tidal interactions.* The user must specify the values of κ and γ for the polytropic EOS, along with the central enthalpies for each NS. We use our own TOV code to ensure that these enthalpies correspond to the desired masses for both NS. The distance between the stars is also specified at this stage, as is the number of collocation points in `Lorene`'s 3-dimensional nested grid structure.

The second stage of the `Lorene` code takes these superimposed TOV solutions and relaxes them using a relaxation factor multiplied by the enthalpy field and each auto-potential from the

current and previous iteration [2], solving for all metric fields self-consistently including tidal interactions. This stage requires the information about the grid, along with a file containing various initial conditions for each star, convergence error thresholds, the number of iterations to perform various tasks, and the relaxation parameters applied as the code moves from iteration to iteration. Lorene reads in all of this information at the beginning of the routine to launch the relaxation code.

3.1.2 Summary of parameter space

In this work, we varied the input physical parameters describing our NS into `Lorene` to see how the code behaves for different γ values, NS masses and radii, and binary separation distances. This was done to document when the code behaves normally and reaches a convergent solution, when it finishes running but diverges, with errors increasing drastically by the end of what should be a relaxation run, and when the code crashed and did not run to completion at all. We considered NS models with γ values ranging from $\frac{5}{3}$ to 3, and NS masses between 1.4 and $1.8 M_{\odot}$. Changing these values can have large effects on the output of the code, and whether it will run to completion or crash. We also tested different separation distances to see how the code performed and to see how binary NS tidal interactions incorporated from one distance to another affect the stability of the relaxation routines.

In what follows, we distinguish between the gravitational mass, which incorporates all of the mass-energy in the NS, including all potential energy effects, and the baryon mass, a sum over the mass of all the particles in the NS. For a non-relativistic object these would be almost exactly equal, but since NSs have non-Newtonian gravitational field strengths, with densities that cause significant bending of space in their vicinity, these values will differ by appreciable amounts.

We have found through our simulations that the `Lorene` code will crash if the initial baryon masses are too high, so we have to start them at a lower value and then gradually increase the mass of each NS once a relaxed configuration is determined at lower mass. In doing so, we effectively allow the NSs to start interacting with each other gradually, enhancing the stability

of the iterative scheme.

`Lorene` uses many iterations to update the mass of the two stars, generally several hundred steps per relaxation calculation. On an ongoing basis, it solves for the spacetime metric field configurations, the enthalpy and velocity state of the matter, and then modifies the zero-point of the enthalpy every few timesteps (this is a user-specified parameter) so that the baryonic mass of the NS is equal to a specified value. After the code has created a stable binary system with the appropriate masses at a given radius, it can then decrease the separation distance and re-solve for the new closer equilibrium configuration.

We have found that if we simply move the stars closer together, the code is unstable for higher-mass configurations, and will often either crash or diverge. If instead we take a lower-mass configuration at the previous separation, move it inward, and again allow the masses to gradually increase, results are often significantly more likely to converge. A big issue with the code is the instability of the relaxation routines for small γ values. `Lorene` has extreme difficulty creating configurations for anything with $\gamma \lesssim 5/3$, and often crashes for $\gamma \lesssim 2$, especially with a higher difference in mass between the two stars.

To better understand the behavior of the code and to try and get it to work for as wide a range of parameter space as possible, we investigated whether relaxation sequences converge for varying input values such as the error threshold and total number of iterations, by running many tests while changing these values to see when the code crashed and when it was successful. The code converges and terminates the calculation when the total relative change in enthalpy summed over all gridpoints in the star, defined as the sum of the pointwise enthalpy differences divided by the pointwise sum over all enthalpy values,

$$\frac{\sum |H^J(x_i) - H^{J-1}(x_i)|}{|\sum H^{J-1}(x_i)|} \tag{3.1.1}$$

where "J" is the step and the summation is over all gridpoint values, is less than a given tolerance over the course of one iteration to the next. Since enthalpy is a function of mass and is used to set the configuration of the star, it is used to check convergence [2]. As the NSs start to stabilize, the change in enthalpy from one iteration to the next should decrease

because large differences in mass cause the code to crash, so it's important that the change in enthalpy becomes very small. After testing, we found that a good threshold for the change in enthalpy is 10^{-7}.

Checking the error that was produced at each separation distance gave a good understanding of how the code performed, along with the ability to see the changing separation distance and growing tidal deformations of the stars due to their interactions. It also showed how the code struggles to handle stars with different masses, particularly for configurations with components of 1.4 to $1.8M_{\odot}$, respectively, the most unequal-mass configurations we considered. Although each star in the binary system had the same EOS (or, equivalently, identical values of κ), changing the NS masses and separation distances still produced significantly different results.

Figs. 3.5, 3.6, 3.7, 3.8, 3.9, and 3.10 show when Lorene crashes and what initial γ and mass values cause the code to crash or diverge and produce inaccurate results. In Fig. 3.5, only the smaller γ values and high mass ratios caused the code to diverge, meaning it could not get below the change in enthalpy of 10^{-7}. This corresponds to the yellow color. The green color corresponds to successful simulations where the change in enthalpy was below 10^{-7} on the last iteration. The red color means the code could not start running due to the fact that the previous separation distance diverged. As the separation distance decreases, Figs. 3.6 and 3.7 show that the trend of low γ values and high mass ratios continue to cause the code to crash or diverge. One reason for this behavior is the fact that Lorene is an iterative process that relies on many approximations, including the TOV simplification. These approximations have some small error contained in them and this error can get magnified over iterations. This is easy to see in Figs. 3.5 and 3.10. Both of these graphs are at the same separation distance, but Fig. 3.10 has significantly less successful runs that Fig. 3.5 since the errors in Fig. 3.10 have had time to accumulate over iterations.

Figs. 3.8, 3.9, and 3.10 also show that small γ values and high mass ratios cause the code to crash and diverge. This is due to the fact that smaller γ values create more compact neutron stars and more compact stars can be unstable. Lorene struggles to simulate stars that

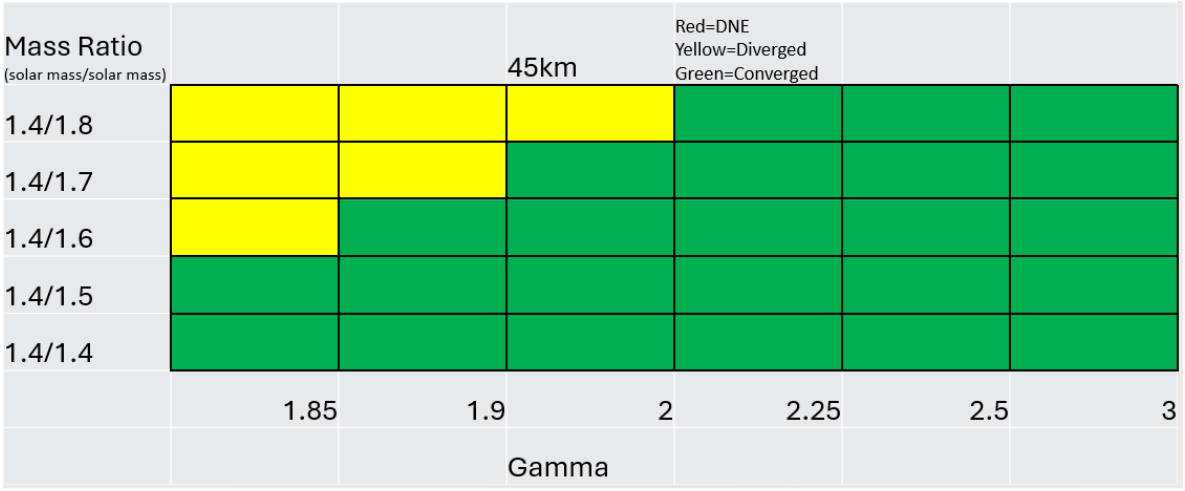

Figure 3.5: Lorene success rate with an initial separation of 45km. The colors correspond to the success of Lorene. Green means the code converged and passed below the change in enthalpy, yellow means the code diverged, it finished running but could not get below the change in enthalpy and red means the code could not even start running. This happens when the previous separation distance diverges. The horizontal axis represents different gamma values used in the TOV code and the vertical axis shows the mass ratio of the binary system.

are unstable or close to the point of instability. High mass ratios further contribute to this problem since more massive stars are more likely to be unstable or close to the stability point.

Figs. 3.11, 3.12 and 3.13 show the extrinsic curvature of the binary NS system, $K^{ij}K_{ij}$, both with masses of $1.4M_{\odot}$, an initial separation distance of 50km and an EOS with $\gamma = 2$ in the $x-y$ plane. Here the x-axis represents the binary axis of the system and the instantaneous momenta for each NS lies in the y-direction. The extrinsic curvature K^{ij} is essentially the partial time derivative of the spatial metric along the normal vector. The breakdown of Lorene's spectral expansion for the NS fields is clear to see in the last plot, in which the separation distance goes down to 45km. The extrinsic curvature is no longer smooth like the two previous versions and appears to have a significant quantity of high-frequency noise. This sudden change in curvature over a distance of 2.5km combined with its non-smooth behavior show signs that the convergence routines used by the code are breaking down.

Figs. 3.14, 3.15 and 3.16 show the Baryon density isocontours in the $x-y$ plane for a NS binary with the same binary NS components as Fig. 3.11, The first graph has a separation distance of 50km, the second is 47.5km and the last is 45km. The breakdown of the code is

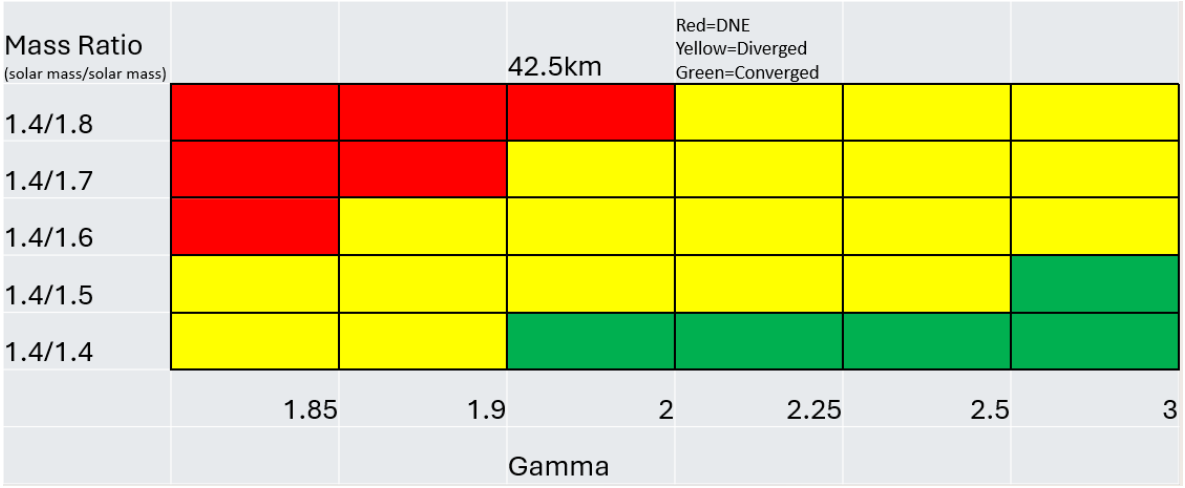

Figure 3.6: Lorene success rate with an initial separation of 45km. Now the separation distance has decreased to 42.5km. conventions are as in Fig. 3.5.

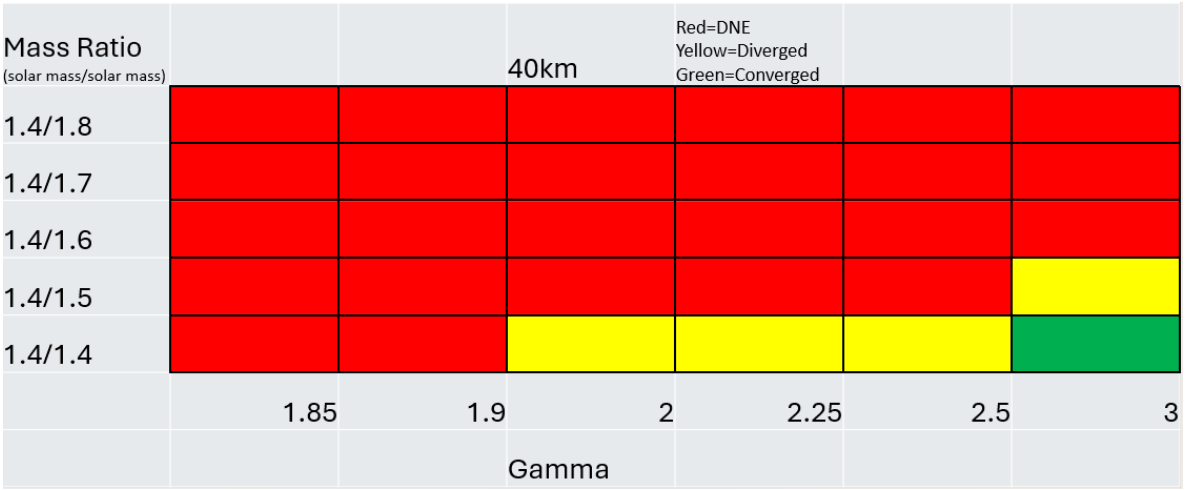

Figure 3.7: Lorene success rate with an initial separation of 45km. Now the separation distance has decreased to 40km. conventions are as in Fig. 3.5.

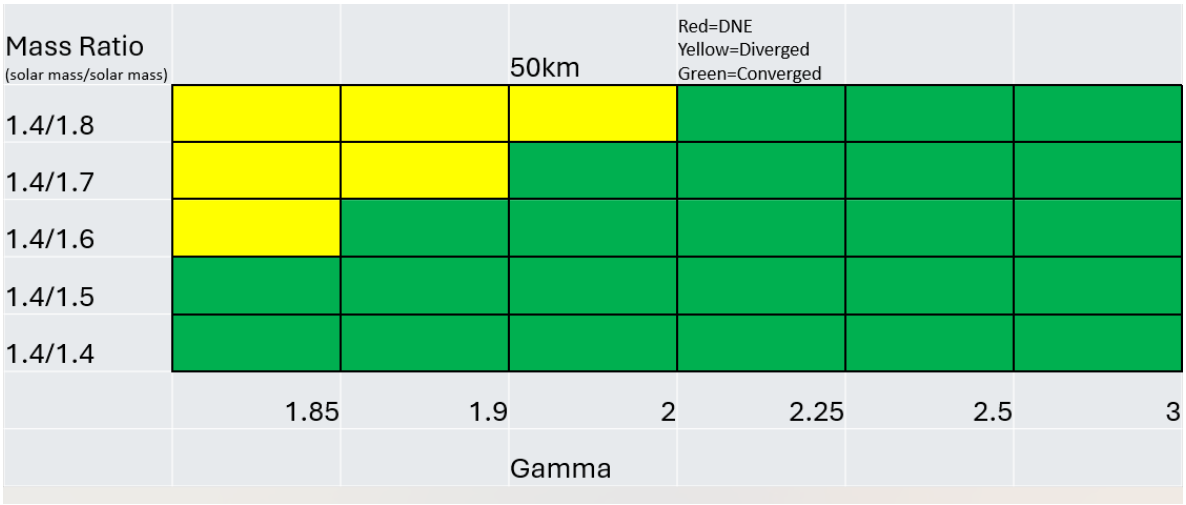

Figure 3.8: Lorene success rate with an initial separation of 50km. conventions are as in Fig. 3.5.

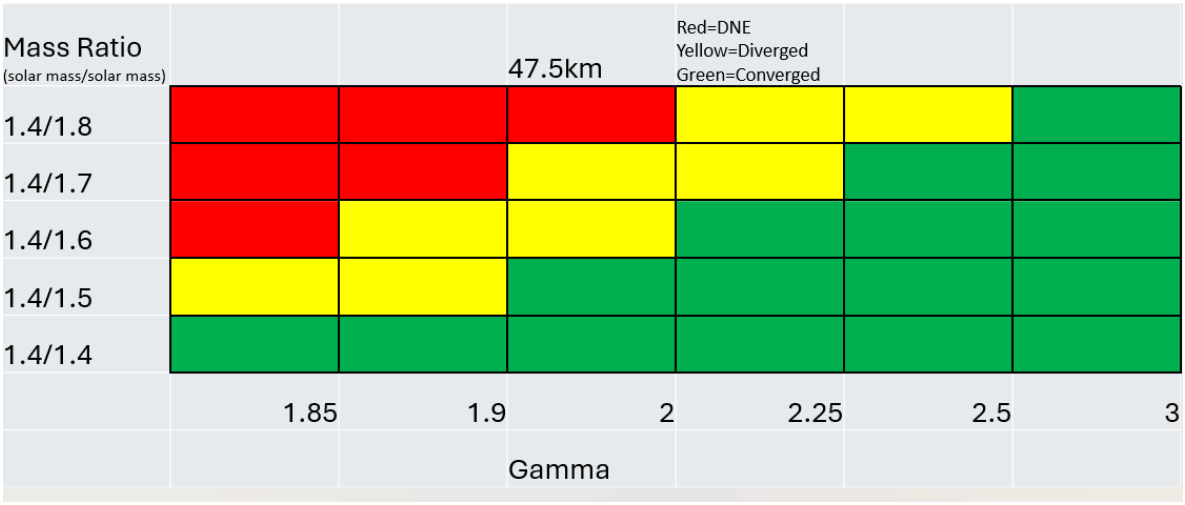

Figure 3.9: Lorene success rate with an initial separation of 50km. Now the separation distance has decreased to 47.5km. conventions are as in Fig. 3.5.

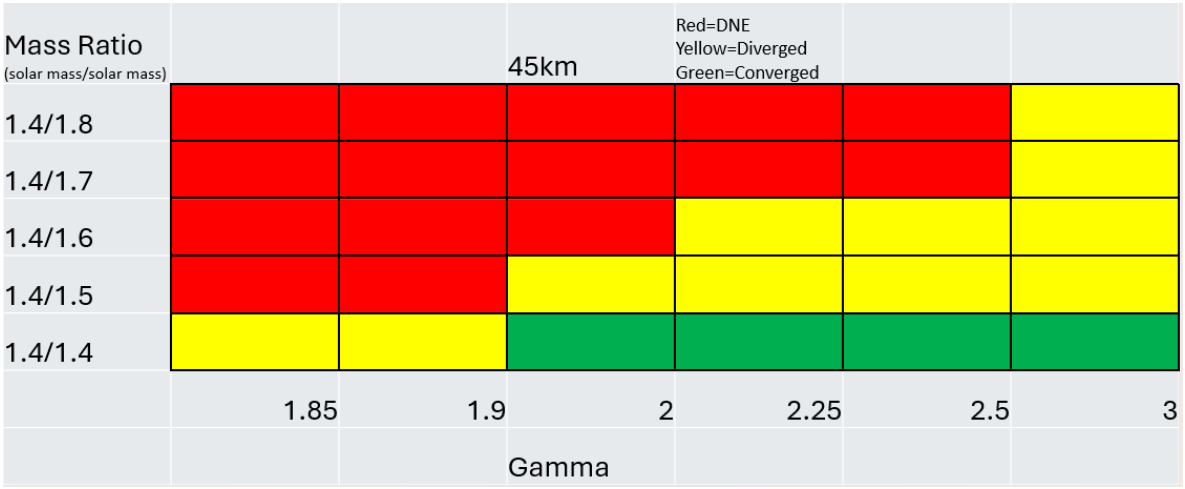

Figure 3.10: Lorene success rate with an initial separation of 50km. Now the separation distance has decreased to 45km. conventions are as in Fig. 3.5.

clear to see at 45km where the isocontours are non-smooth. This is due to the fact that the spectral expansion in the θ-direction is no longer accurate, due to the presence of substantial contributions of high-frequency components.

Figs. 3.17, 3.18, 3.19 show the shift vector in the $x-y$ plane for a NS binary with the same binary NS components as Fig. 3.11. The shift vectors shows, relative to the normal vector, how the spatial coordinates evolve in time. Although the directions of the shift vectors do not seem to diverge or change substantially by the end, the shape of the NS still indicates that the code has become wildly inaccurate. One reason why the vectors appear to be fairly consistent is that the velocity model is specified, and thus the shift vector is less susceptible to high-frequency noise, whereas the extrinsic curvature, defined in terms of *derivatives* of the shift vector, preferentially amplifies the small-amplitude but high-frequency components present in the data [2].

Figs. 3.20, 3.21, 3.22, 3.23, 3.24, 3.25 show the enthalpy isocontours in the $x-z$ and $x-y$ planes for a NS binary with the same binary NS components as Fig. 3.11. The last plot shows that the majority of the error is in the ϕ-direction, with the θ-direction (shown at $z=0$)

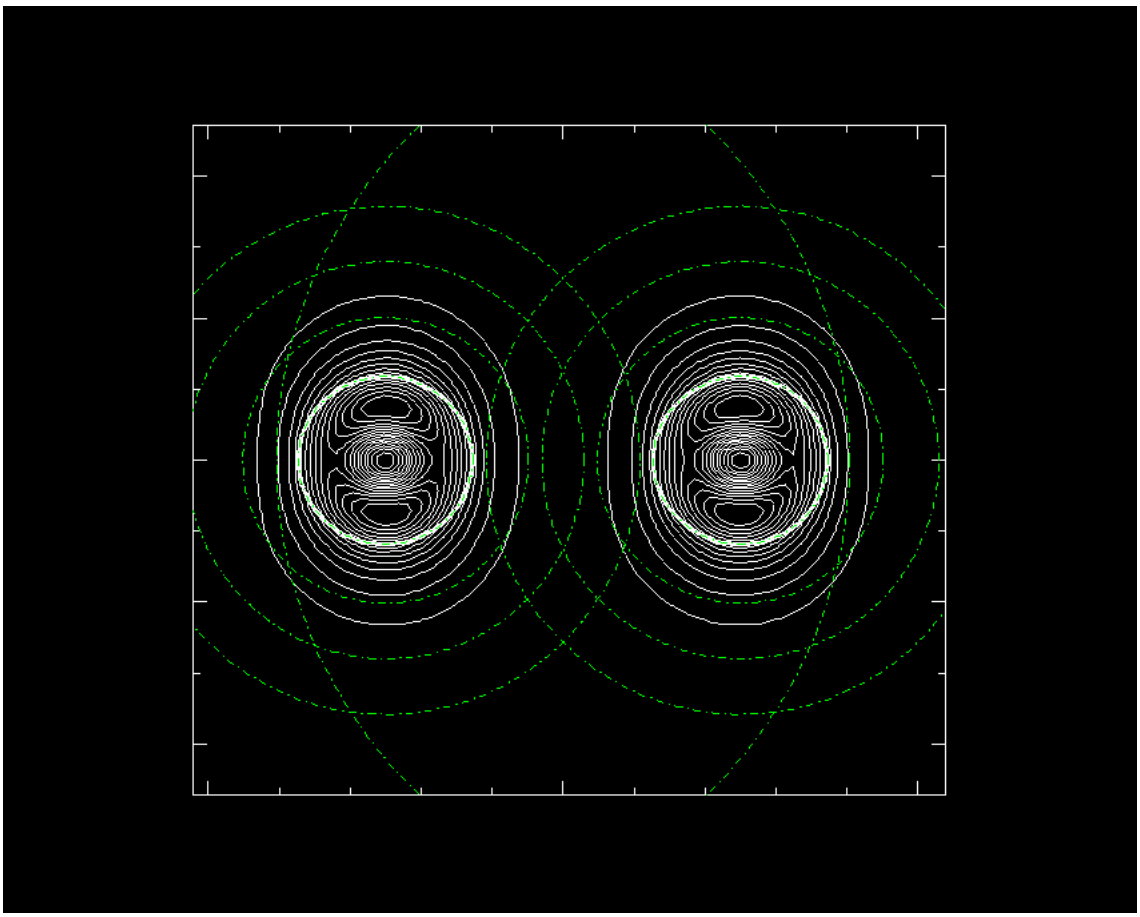

Figure 3.11: Extrinsic curvature $K^{ij}K_{ij}$ isocontours at 50km for a binary NS system with both NS having masses of $1.4M_{\odot}$ and a NS EOS with $\gamma = 2$ shown in the $x-y$ plane. The NS surface is shown as a heavy solid line. Lorene grid domain boundaries are shown as dashed green curves, and surround each NS, with both sets extending throughout all space.

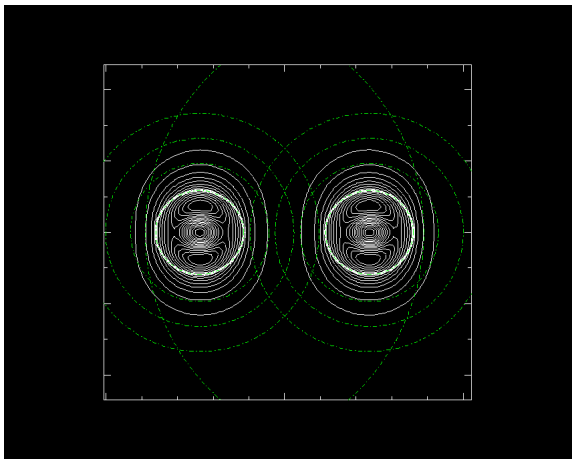

Figure 3.12: Extrinsic curvature isocontours at 47.5km in the $x-y$ plane, for a binary system with NS components equivalent to those in Fig. 3.11

.

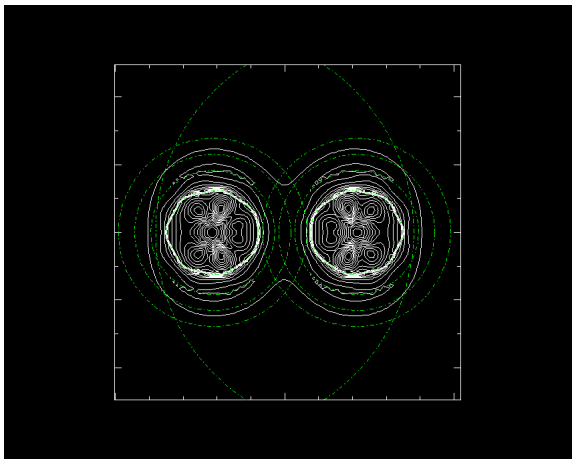

Figure 3.13: Extrinsic curvature isocontours at 45km in the $x-y$ plane, for a binary system with NS components equivalent to those in Fig. 3.11.

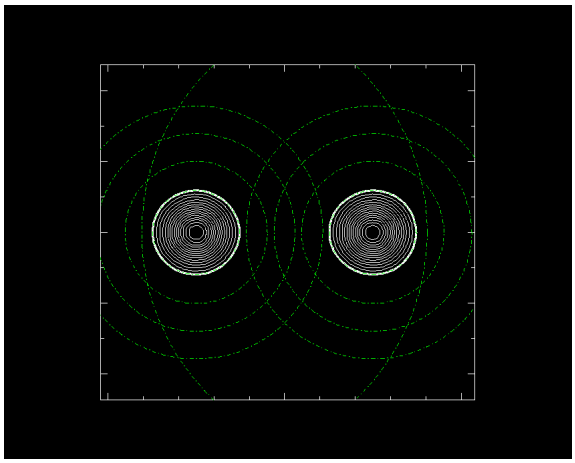

Figure 3.14: Baryon density isocontours at 50km in the $x-y$ plane, for a binary system with NS components equivalent to those in Fig. 3.11

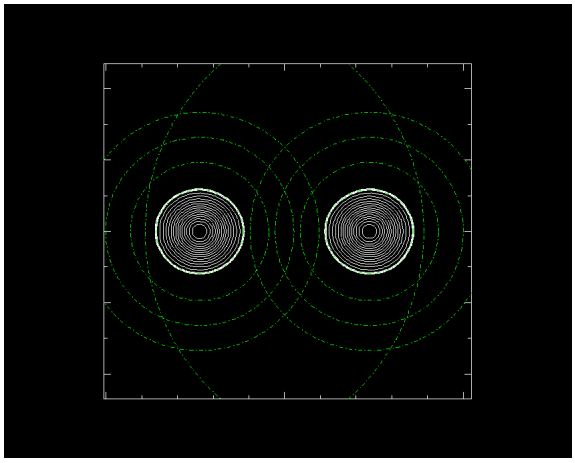

Figure 3.15: Baryon density isocontours at 47.5km in the $x-y$ plane, for a binary system with NS components equivalent to those in Fig. 3.11.

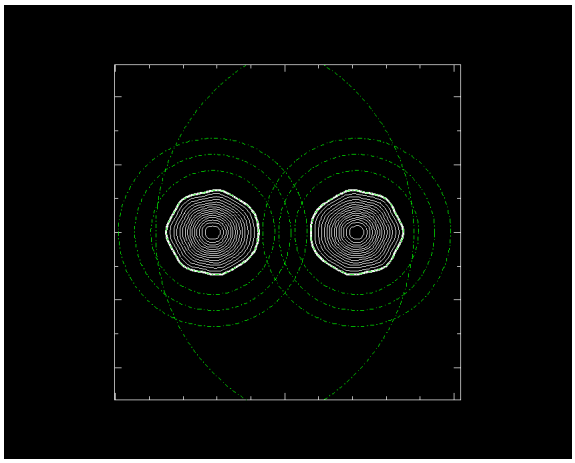

Figure 3.16: Baryon density isocontours at 45km in the $x-y$ plane, for a binary system with NS components equivalent to those in Fig. 3.11.

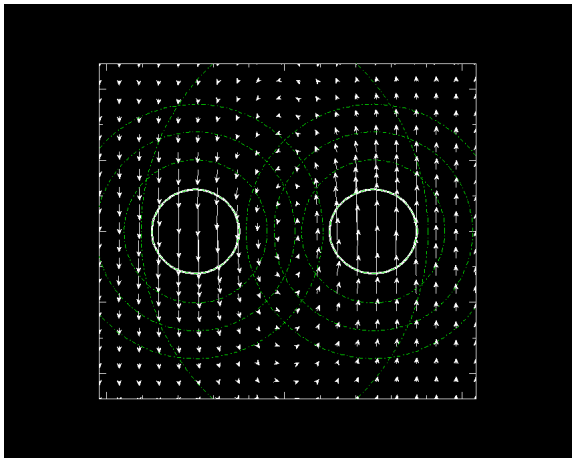

Figure 3.17: Shift vector at 50km in the $x-y$ plane, for a binary system with NS components equivalent to those in Fig. 3.11.

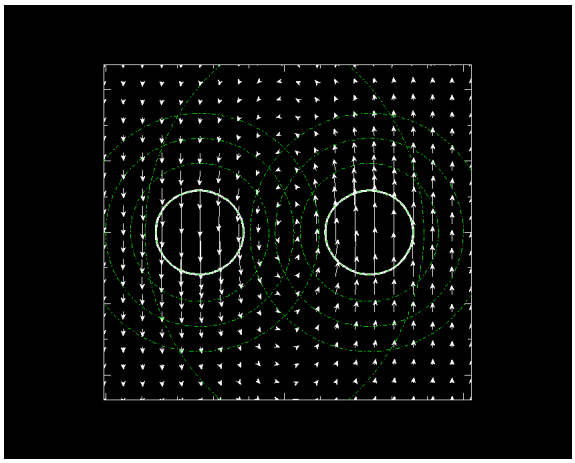

Figure 3.18: Shift vector at 47.5km in the $x-y$ plane, for a binary system with NS components equivalent to those in Fig. 3.11.

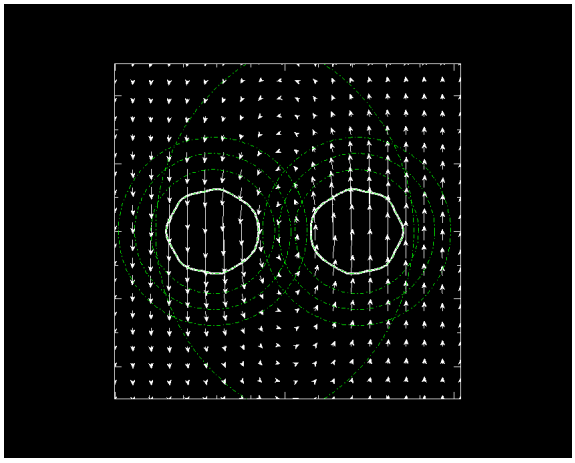

Figure 3.19: Shift vector at 45km in the $x-y$ plane, for a binary system with NS components equivalent to those in Fig. 3.11.

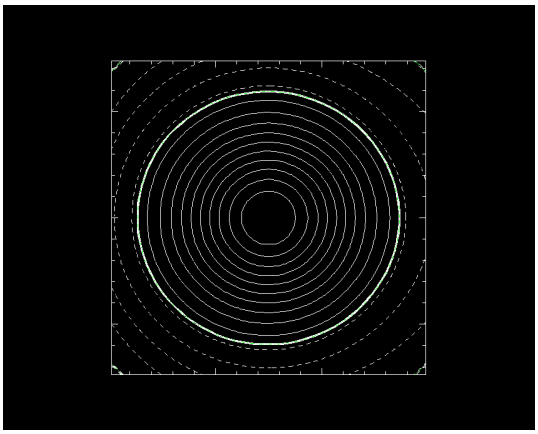

Figure 3.20: Enthalpy isocontours in the $x-z$ plane at 50km, for a binary system with NS components equivalent to those in Fig. 3.11.

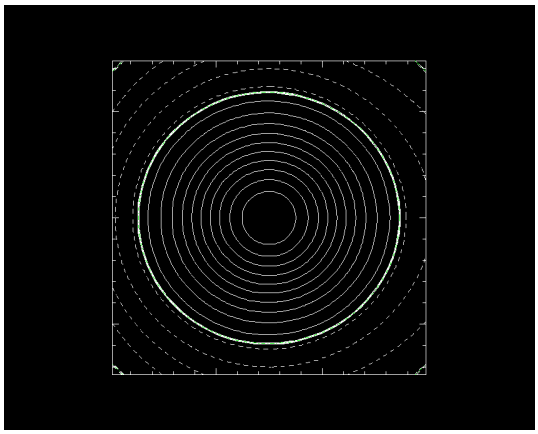

Figure 3.21: Enthalpy isocontours in the $x-y$ plane at 50km, for a binary system with NS components equivalent to those in Fig. 3.11.

yielding smoother results when compared to sections taken in the $x-z$ plane. The ϕ-direction errors are likely so large that they are in some sense the cause of some error in the θ-direction as well. The error is caused by large terms in the high-frequency Fourier series expansion of the surface equation. The extreme oscillations in these terms are distorting the surface of the NSs, which effects every part of the equilibrium-finding routines that follow. The θ-direction also has some clear error, but at a noticeably smaller level.

Even though technically the code converged for a model with an EOS with $\gamma = 2$, equal NS masses of $1.4M_{\odot}$, and an initial separation distance of 50km, with an iteration-to-iteration change in enthalpy value below the threshold, these inaccurate results are consistent with a run that failed to converge to a valid physical solution, Figs. 3.26 and 3.27, with a γ value of 2.25, equal masses of $1.4M_{\odot}$ and an initial separation distance of 45km. The inaccurate results of Figs. 3.26 and 3.27 occurred when the separation distance decreased to 40km.

Lorene's initial accuracy is very high, but it is not perfect. In modeling the surface shapes of NSs, the code eventually allows for significant amplitudes in the modes describing the surface, where the enthalpy goes to zero. These approximations can eventually lead to significant errors when they begin to act as source terms for the field equations.

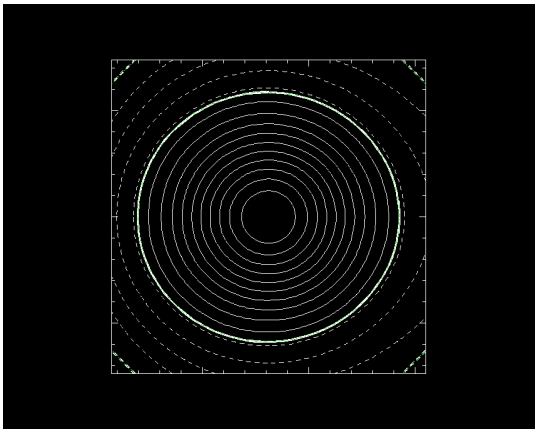

Figure 3.22: Enthalpy isocontours in the $x-z$ plane at 47.5km, for a binary system with NS components equivalent to those in Fig. 3.11.

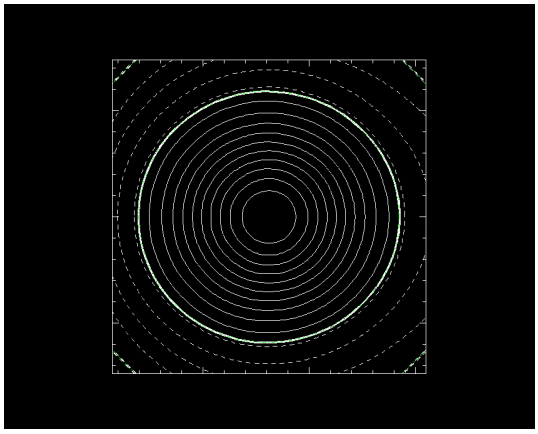

Figure 3.23: Enthalpy isocontours in the $x-y$ plane at 47.5km, for a binary system with NS components equivalent to those in Fig. 3.11.

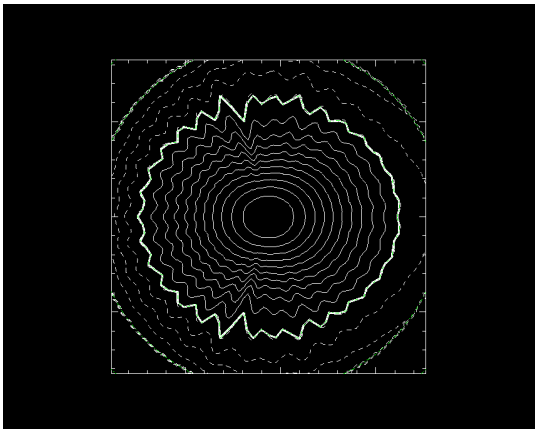

Figure 3.24: Enthalpy isocontours in the $x-z$ plane at 45km, for a binary system with NS components equivalent to those in Fig. 3.11.

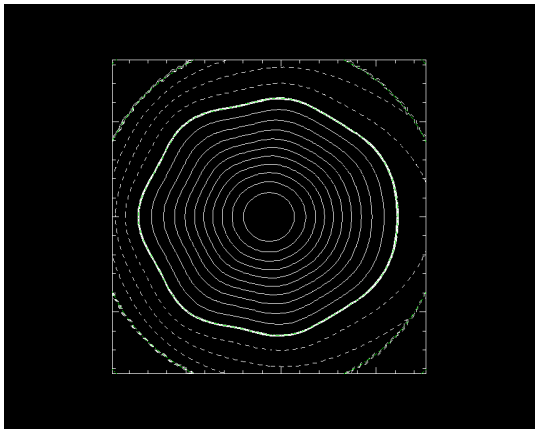

Figure 3.25: Enthalpy isocontours in the $x-y$ plane at 45km, for a binary system with NS components equivalent to those in Fig. 3.11.

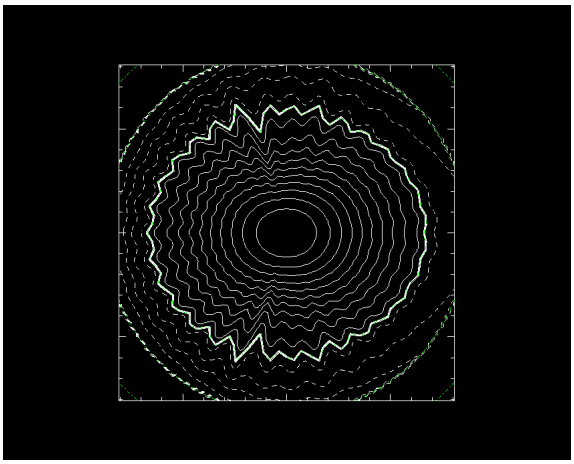

Figure 3.26: Inaccurate enthalpy isocontours in the $x - z$ plane at 40km, causing the code diverge. for a binary NS system with both NS having masses of $1.4M_{\odot}$, an EOS with $\gamma = 2.25$ and an initial separation distance of 45km.

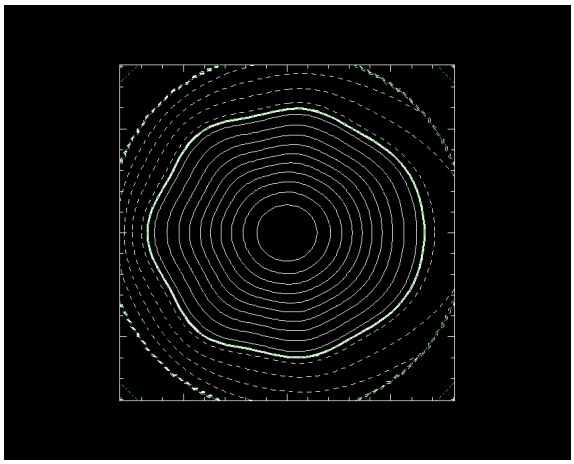

Figure 3.27: Inaccurate enthalpy isocontours in the $x - y$ plane at 40km, causing the code diverge. for a binary NS system with both NS having masses of $1.4M_{\odot}$, an EOS with $\gamma = 2.25$ and an initial separation distance of 45km.

Moreover, our runs are more stable at a given separation if that separation is used as an initial distance for the code, rather than serving as the second or third model in a sequence of increasingly close binary configurations. Apparently, the reason that an initial separation distance of 45km produced more successful runs than the third iteration of runs with an initial distance of 50km (now at 45km) is likely due to the fact that each successful iteration of Lorene is built off of the previous one, with errors accumulating rather than being properly relaxed away. If the previous iteration has high-frequency noise present at all, the new one will not be as accurate as the previous because it will compound the errors already present in the previous steps. Possible underdamping in the relaxation scheme can produce overshooting of the metric fields as the stars settle into their new equilibrium configuration [3]. This limits the overall ability of the code to generate sequences as the separation distance for a given binary is decreased.

Chapter 4

BH light deflection

4.1 Light deflection in black hole spacetimes

Previous work by the RIT group has focused on developing approximate techniques for calculating the deflection of photon trajectories in the equatorial plane of Kerr BHs, including both the total deflection [5] and the full trajectory in space [31]. Here, we take the full 4-dimensional spacetime geodesic equations for Kerr-Newman BHs [4], i.e., BHs with arbitrary spin and charge, and consider the effects of BH gravity on photons not necessarily confined to the equatorial plane.

4.2 Non-equatorial geodesics

In this thesis, we consider primarily Kerr BHs, with charge set to zero. We note this is the physically realistic case, with electric charge largely considered in the literature for mathematical rather than practical interest. To simplify the models being considered, we begin evolving photon trajectories from a point located in the equatorial plane ($\theta = \pi/2$), defining this to be $\phi = 0$ in the azimuthal direction. In previous works, the photon direction was chosen to lie in the equatorial plane as well; here we can compare that case for our simulations to results obtained in previous papers [4, 5, 31].

4.3 Light deflection: results

While our evolution code for the photon geodesic trajectories is a fourth-order RK4 scheme, we see different convergence behaviors for some particular cases. In particular, We see fourth order convergence with RK4 for any initial direction ϕ that is *not* tangential to the BH, $\phi \neq \pi/2$, with first order convergence for that particular case, $\phi = \pi/2$.

The reason is simple, if somewhat complicated to avoid. For photons that start off with no initial radial velocity, there is a singularity in the right hand side of Eq. (2.4.3) ($\frac{dr}{d\sigma}$), which involves the square root of a function with linear radial dependence. As such a term is not smooth, nor even singly differentiable, convergence drops to first order for simulations begun on these trajectories (formally speaking, the RHS terms are not Lipschitz continuous in that case). We have confirmed first-order convergence for runs begun with $\phi = \pi/2$, and fourth-order convergence for photon trajectories with all other initial directions. In either case, we mau use Richardson extrapolation to yield high-accuracy results, so long as we incorporate the correct convergence order into the formula.

We found that evolving the path in spherical coordinates was also problematic for this particular case. Indeed, having $\frac{dr}{d\sigma}$ initially zero violates the assumptions about unique solutions for differential equations (DEs), since the derivative of the right hand side of the DE with respect to radius is not smooth under these conditions. To solve this problem, we evaluated all derivatives in spherical coordinates, and converted these into Cartesian displacements for the photon's path using Eqs. (2.4.7)- (2.4.9), converting the new positions back to spherical coordinates again to evaluate the RHS of Eqs. (2.4.3) - (2.4.6) at every step. The use of Cartesian calculations did not change the first order behavior when ϕ was aimed tangentially to the BH.

An error analysis was conducted to determine the accuracy of the code in each dimension. We began with an initial step size of 2×10^{-8} and continuously halved the step size. We then calculated the absolute value of the difference between the original step size and half the step size, half the step size and a quarter, and so on. The first curve (original step size minus half the step size, ε_i) should be 16 times larger than the next curve (ε_{i+1}) since RK4 is fourth

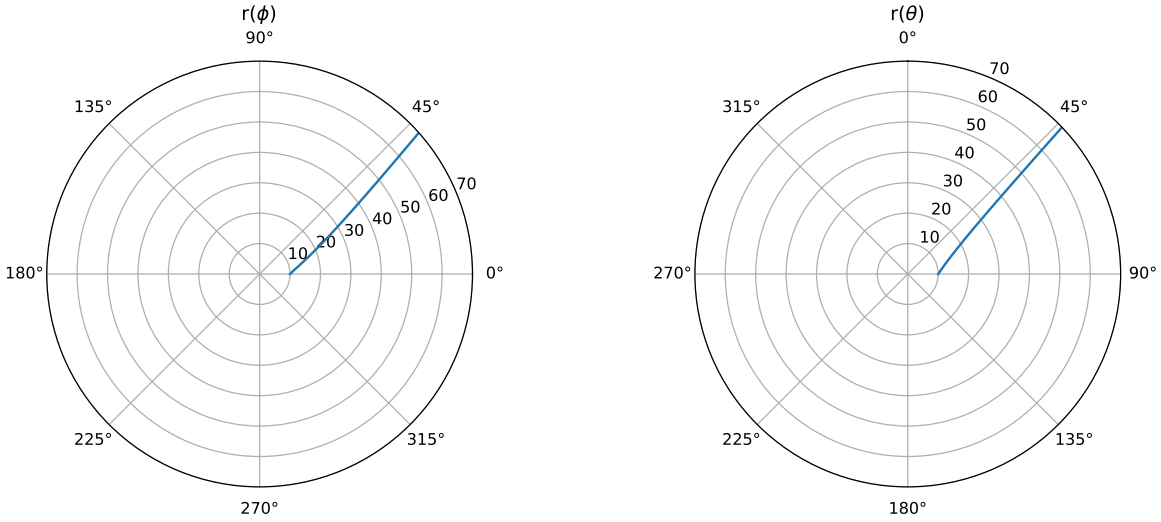

Figure 4.1: Photon's path in the equatorial plane (left) and vertical plane (right) at an initial distance of 10 times the BH's, radius with no spin. The photon's initial direction is $\phi = \frac{\pi}{4}$ and $\theta = \frac{\pi}{4}$

order accurate, $\lim_{h\to 0} \frac{\varepsilon_i}{\varepsilon_{i+1}} = 2^n$, n = convergence order and h = step size. This is why the radial, phi and theta convergence plots of Figs. 4.2 - 4.4 have curves that are approximately equal to 16. The sharp spikes that appear in the convergence plots of Figs. 4.2 - 4.4 around $\sigma = 0.08$ result from a zero-crossing in the leading order-error term, the location of which itself converges at fourth-order. While the typical assumptions about the scales of the error terms at various orders do not hold instantaneously, we see results completely consistent with fourth-order convergence throughout the duration of the evolution plotted.

Figs. 4.5-4.7 show the change in the final phi direction over different initial theta directions. These are used to analyze the effects of spin on a photon's path outside of the equatorial plane. Noting that we have symmetry for photons whose trajectories lie above or below the equatorial plane, the final phi direction can be approximated with an expansion series involving only even powers of the initial theta direction, θ.

$$\phi_f(\theta) \approx \phi_f\left(\theta = \frac{\pi}{2}\right) + \kappa\left(\theta - \frac{\pi}{2}\right)^2 + \beta\left(\theta - \frac{\pi}{2}\right)^4 + ... \tag{4.3.1}$$

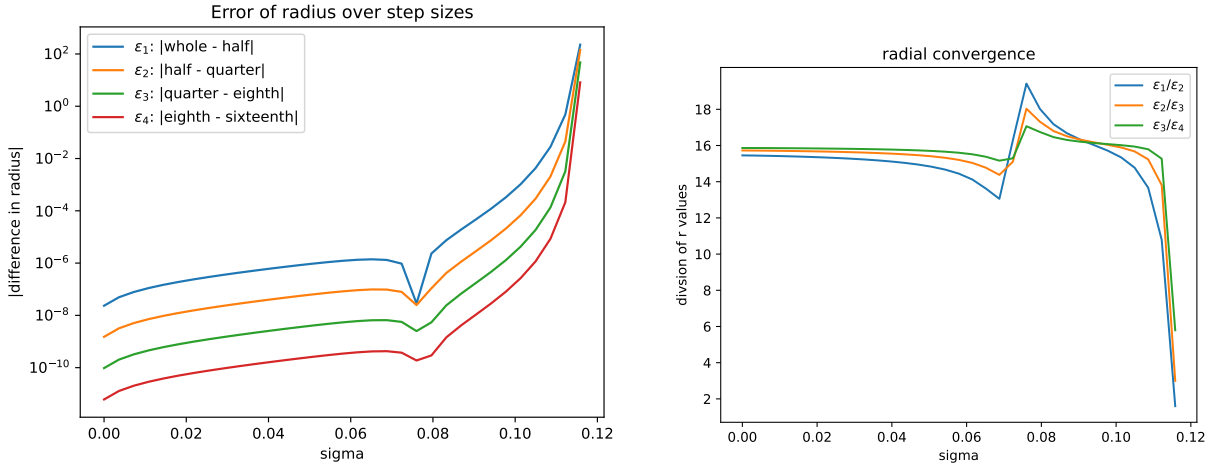

Figure 4.2: Differences in radius, as a function of the affine parameter σ that serves as a proxy for path length (see Eq. 2.4.3), between models computed using varying stepsizes (left). Initial data is the same as in Fig. 4.1. A calculation of radial convergence (right) was obtained from dividing by the photon's path over different step sizes. A value of 16 is expected for fourth-order convergence. The spike present around $\sigma \sim 0.08$ results from a sign change in the lowest-order error term, with the expected fourth-order convergence observed both before and after the crossing.

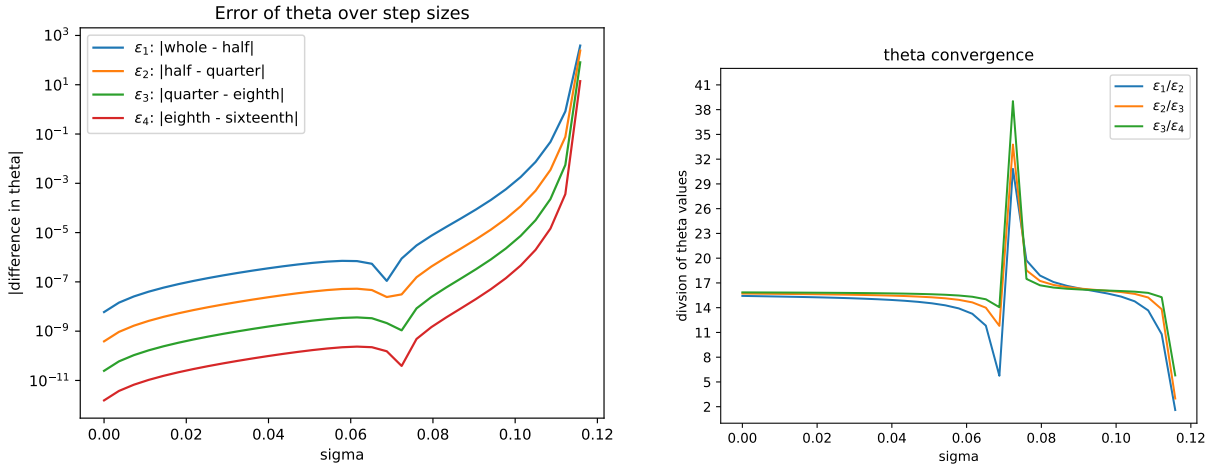

Figure 4.3: A calculation of differences in theta values over smaller step sizes (left). Initial data is the same as in Fig. 4.1. A calculation of radial convergence (right) was obtained from dividing by the photon's path over different step sizes. A value of 16 is expected for fourth-order convergence. The spike present around $\sigma \sim 0.08$ results from a sign change in the lowest-order error term, with the expected fourth-order convergence observed both before and after the crossing.

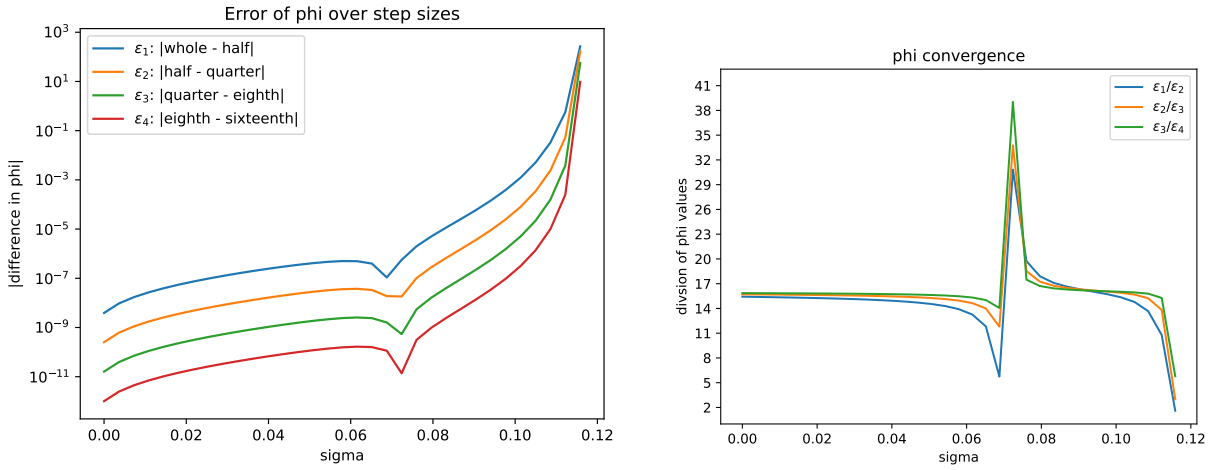

Figure 4.4: A calculation of differences in phi values over smaller step sizes (left). Initial data is the same as in Fig. 4.1. A calculation of radial convergence (right) was obtained from dividing by the photon's path over different step sizes. A value of 16 is expected for fourth-order convergence. The spike present around $\sigma \sim 0.08$ results from a sign change in the lowest-order error term, with the expected fourth-order convergence observed both before and after the crossing.

Here, κ and β are constants, whose value can be approximated from numerical runs, and the zeroth order term, $\phi_f\left(\theta = \frac{\pi}{2}\right)$, can be determined from our numerical simulations directly. To find the values of κ and β, We plotted Eq. (4.3.2) against $(\theta - \frac{\pi}{2})^2$ and calculated a linear fit. The line of best fit is plotted to show the second order coefficient and y-intercept, κ, and the fourth order coefficient and slope, β. Each plot has a different initial radius and the larger radii have smaller slopes for their best fit lines. This is due to the fact that the black hole's gravity has less of an effect at larger distances.

$$\frac{\phi_f(\theta) - \phi_f\left(\theta = \frac{\pi}{2}\right)}{\left(\theta - \frac{\pi}{2}\right)^2} = \kappa + \beta\left(\theta - \frac{\pi}{2}\right)^2 \tag{4.3.2}$$

Table 4.1 shows the slope, β, and y-intercept, κ, of the final phi directions over different initial theta directions. Displaying multiple plots over different initial radii allows us to examine how the final bending angle behavior changes as initial radius changes. In Figs. 4.5-4.7, we found that the β and κ values fall off roughly proportionally to $\frac{1}{r_0}$, where r_0 is the initial radius. This makes sense because larger initial separations from the black hole should have

less directional bending. It is also clear to see the BH's spin affecting the bending angle coefficients, κ and β. Retrograde trajectories have larger bending angle coefficients than orbits with no spin and prograde trajectories having the smallest coefficients.

The κ and β dependence on spin at a fixed r_0 was also examined in figure 4.8. From our results, we see the expected roughly linear dependence of the light bending parameter β on the BH spin. There are no symmetries or other special cases present, so the lowest-order variations occur at first-order. The dependence on spin is as expected, if counterintuitive: positive spins (prograde trajectories) yield smaller azimuthal bending angles, whereas negative spins (retrograde trajectories) yield larger ones. As we expected, κ is not symmetric about $a = 0$ since there are no symmetries present. κ surprisingly also has a quadratic dependence on spin that increases until about $a = -0.6$ and then starts to decrease. The explanation for this quadratic dependence is not known and should be further investigated in the future.

The key insight is that all frame-dragging effects occur in the tangential direction, with prograde photons being given boosts in the forward direction, leading to reduced interaction time in the potential well of the black hole, and vice versa. Here, prograde frame-dragging essentially boosts the photon more rapidly out of the potential well, and retrograde frame-dragging slows down the interaction, leading to a longer interaction during the pericenter passage.

	a=-0.5	
r_0	β	κ
9.5	0.0618	0.1347
10	0.0576	0.1260
10.5	0.0540	0.1184
11	0.0508	0.1117
11.5	0.0500	0.1074
12	0.0455	0.1003

	a=0	
r_0	β	κ
9.5	0.0587	0.1240
10	0.0557	0.1245
10.5	0.0524	0.1171
11	0.0494	0.1105
11.5	0.0468	0.1045
12	0.0445	0.0994

	a=0.5	
r_0	β	κ
9.5	0.0569	0.1279
10	0.0535	0.1203
10.5	0.0506	0.1136
11	0.0479	0.1076
11.5	0.0454	0.1021
12	0.0433	0.0972

Table 4.1: The β values represent the slope of the linear fit used to model the final phi direction over different initial theta directions, while the κ values represent the y-intercepts of those linear fits. The calculations were performed for different initial radii starting at 9.5 and ending at 12, and for different spin values.

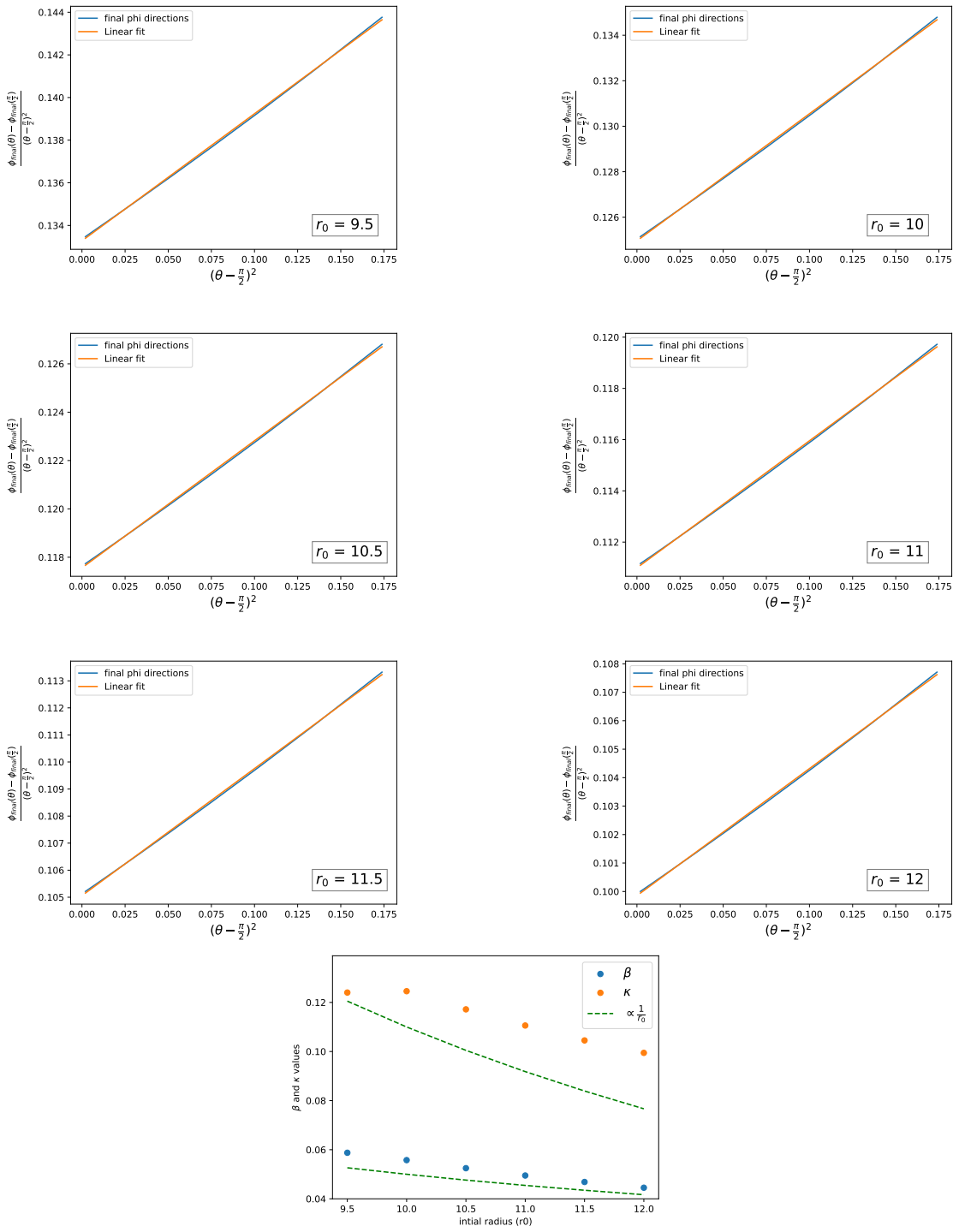

Figure 4.5: The final phi directions plotted over different initial theta directions where spin is set to 0. Each plot contains a linear fit for a set initial radius (r_0). The bottom figure shows how the slope (β) and y-intercept (κ) of each linear fit change over initial radius and how they decrease proportionally to $\frac{1}{r_0}$.

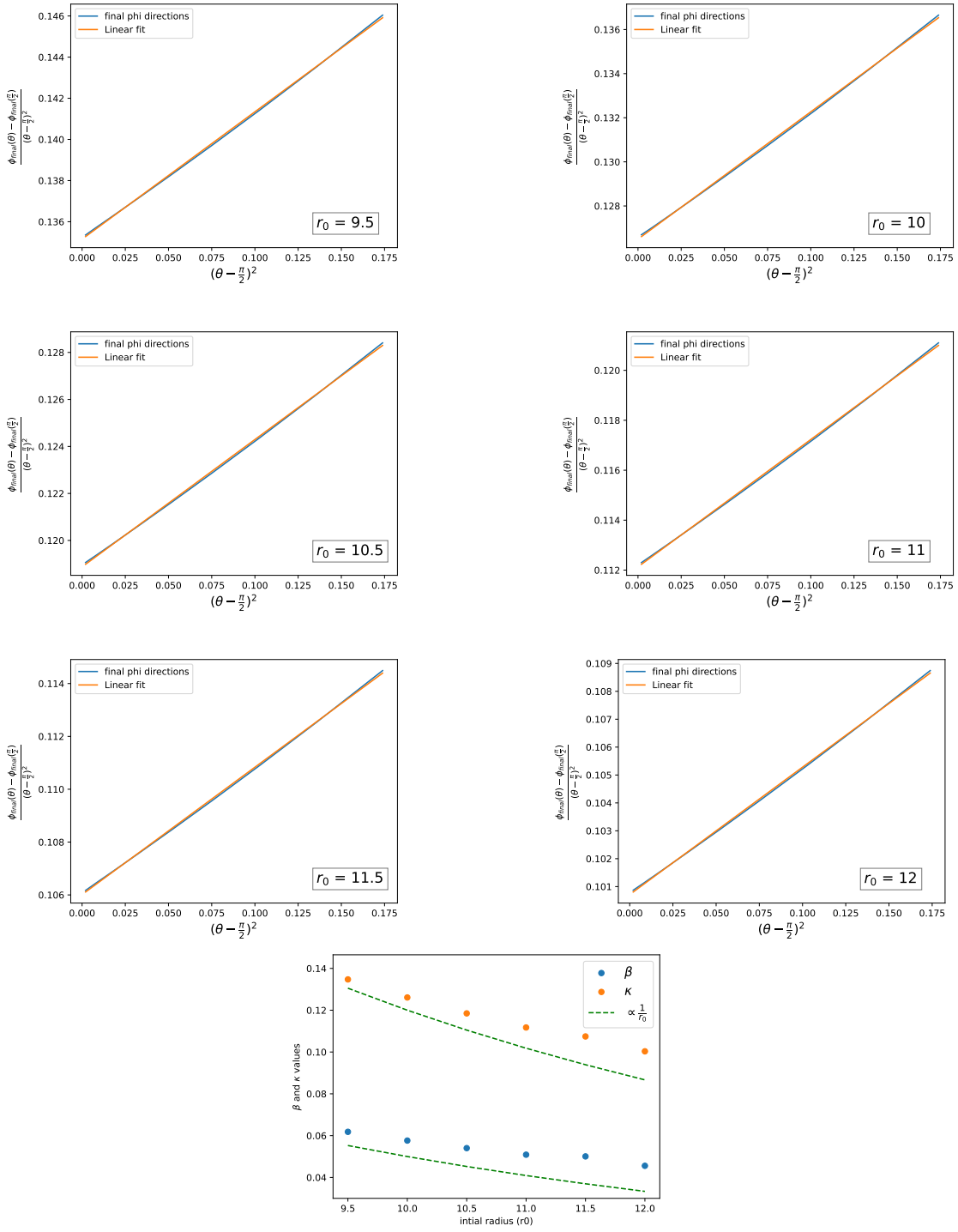

Figure 4.6: The final phi directions plotted over different initial theta directions where spin is set to -0.5. Each plot contains a linear fit for a set initial radius (r_0). The bottom figure shows how the slope (β) and y-intercept (κ) of each linear fit change over initial radius and how they decrease proportionally to $\frac{1}{r_0}$.

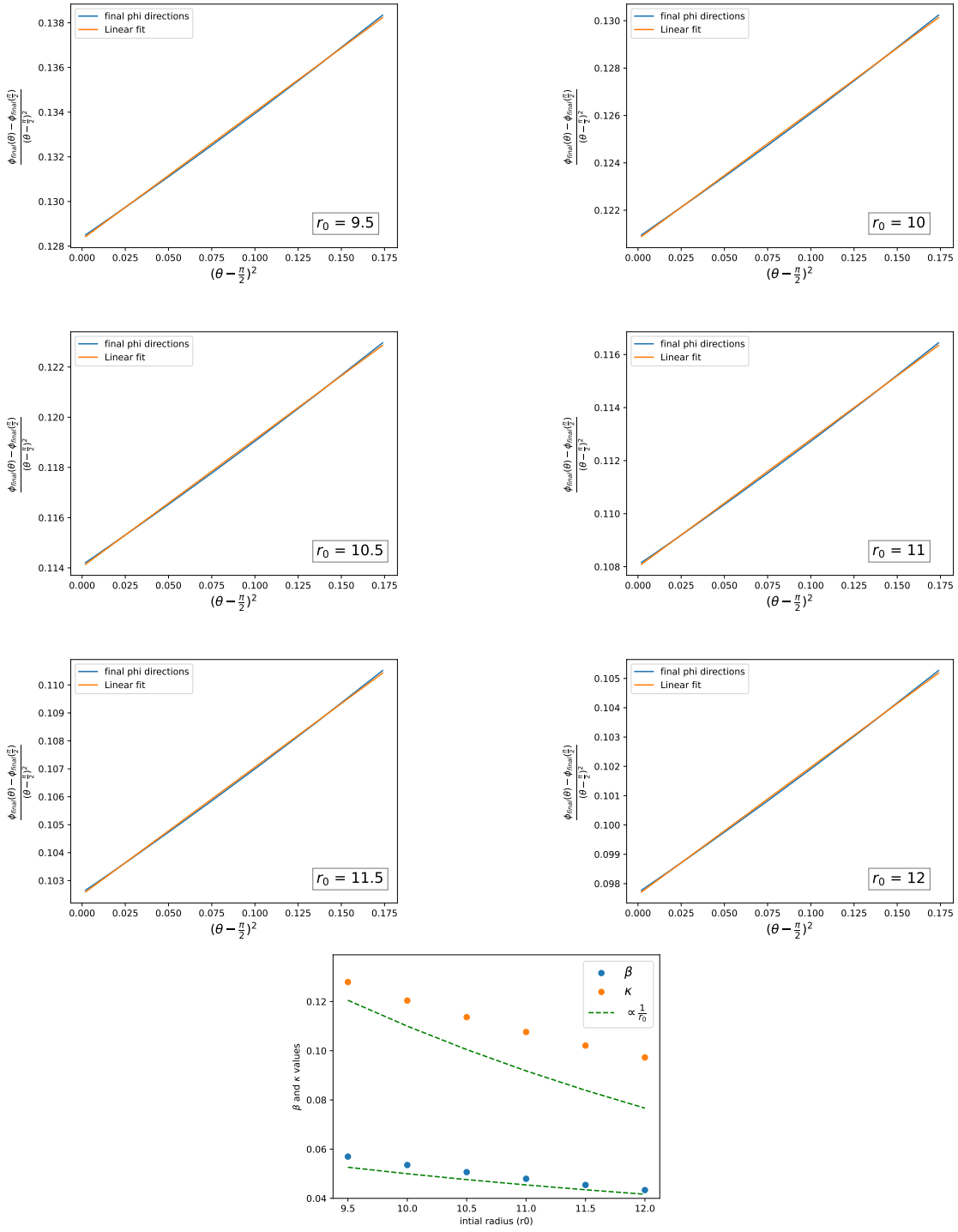

Figure 4.7: The final phi directions plotted over different initial theta directions where spin is set to 0.5. Each plot contains a linear fit for a set initial radius (r_0). The bottom figure shows how the slope (β) and y-intercept (κ) of each linear fit change over initial radius and how they decrease proportionally to $\frac{1}{r_0}$.

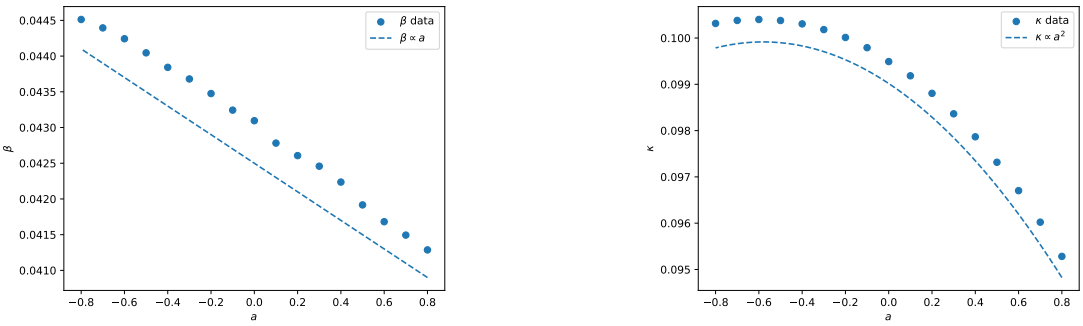

Figure 4.8: The κ and β dependence over different spin values where $r_0 = 12$. β is roughly linear over the full range while κ seems to show roughly quadratic behavior and the explanation for this is not currently present.

Chapter 5

Conclusion

5.1 Conclusion

Since compact objects are often hard to observe or even detect, many astrophysicists rely on powerful simulations to test theories about their properties. The study of compact objects will be of great interest in the future due to their ability to produce gravitational waves. Increased observations and gravitational wave detectors in the future will allow astrophysicists to further study compact objects to fully understand them.

In this thesis we varied the central density of NS in the TOV code to generate initial data. Then used that initial data to find out what values for things such as γ, mass and κ cause `Lorene` to crash, and even showed that some configurations can get below the error threshold and still have results comparable to those that diverged and were above the error threshold.

Moving forward, while `Lorene` remains an interesting candidate code for generating additional relativistic binary initial data, in particular for the still poorly explored phase-space of neutron star-black hole binaries, the complicated nature of its convergence behavior may tilt the balance toward the use of other codes now publicly available within the numerical relativity community.

For the BH light bending simulation, we investigated the bending of a photon's path around a black hole and showed that something as simple as RK4 can have accuracy issues when aiming the photon tangentially. We did the first systematic exploration out of the

equatorial plane and found roughly the expected radial dependence on the bending angle, but there is evidence that the spin dependence for the lowest order behavior in inclination angle may be non-trivial and possibly non-monotonic at high spin.

5.2 Future Work

A deep investigation into the error threshold of Lorene is necessary to understand why it allows some inaccurate values to get below a user specified threshold. Testing `Lorene` on more initial data is recommended because it may help find the cause of this problem.

Future work can also be done on the light bending calculation by testing the effect of charge on the photon's path. More work is necessary to explore the κ and β dependence on spin by testing their behavior over more r_0 values as well as testing more extreme spin values. A deeper investigation into the κ dependence over different spin values should be explored in future works to understand the quadratic behavior and provide further code validation if the same dependencies are found.

Bibliography

[1] D. R. Lorimer and M. Kramer. *Handbook of Pulsar Astronomy*, volume 4. 2004. (document), 1.2.1, 1.1

[2] Eric Gourgoulhon, Philippe Grandclément, Keisuke Taniguchi, Jean-Alain Marck, and Silvano Bonazzola. Quasiequilibrium sequences of synchronized and irrotational binary neutron stars in general relativity: Method and tests. *Physical Review D*, 63(6), February 2001. (document), 1, 2.2, 2.2, 2.1, 3.1.1, 3.1.2, 3.1.2

[3] Tanmayee Gupte. Initial data generation and dynamical simulations of binary neutron star systems, 2022. 1, 3.1.1, 3.1.2

[4] Chen-Yu Wang, Da-Shin Lee, and Chi-Yong Lin. Null and timelike geodesics in the kerr-newman black hole exterior. *Physical Review D*, 106(8), October 2022. 1, 1.3, 1.3.37, 2.4, 4.1, 4.2

[5] Nathaniel S Barlow, Steven J Weinstein, and Joshua A Faber. An asymptotically consistent approximant for the equatorial bending angle of light due to kerr black holes. *Classical and Quantum Gravity*, 34(13):135017, jun 2017. 1, 4.1, 4.2

[6] Saul A. Teukolsky Stuart L. Shapiro. *Black holes, white dwarfs, and neutron stars: the physics of compact objects*. Wiley, first printing edition, 1983. 1.1, 1.2.1, 1.3, 2.1.1

[7] James B. Hartle. *Gravity : an introduction to Einstein's general relativity*. 2003. 1.1

[8] Duncan R. Lorimer. Binary and millisecond pulsars, 2005. 1.2.1, 1.2.4

[9] Jocelyn S. Read, Charalampos Markakis, Masaru Shibata, Kōji Uryū, Jolien D. E. Creighton, and John L. Friedman. Measuring the neutron star equation of state with gravitational wave observations. *Physical Review D*, 79(12), June 2009. 1.2.1, 1.2.3

[10] Wynn C. G. Ho, M. J. P. Wijngaarden, Philip Chang, Craig O. Heinke, Dany Page, Mikhail Beznogov, and Daniel J. Patnaude. Cooling of the cassiopeia a neutron star and the effect of diffusive nuclear burning. 2019. 1.2.1

[11] Frederick M. Walter. Discovery of a nearby isolated neutron star, 1996. 1.2.1

[12] S. A. Rappaport E. P. J. Heuvel. *X-Ray Binaries and Recycled Pulsars*. Springer Dordrecht, 1992. 1.2.1

[13] Bülent Kiziltan, Athanasios Kottas, Maria De Yoreo, and Stephen E. Thorsett. The neutron star mass distribution. *The Astrophysical Journal*, 778(1):66, November 2013. 1.2.1

[14] Feryal Özel, Dimitrios Psaltis, Ramesh Narayan, and Antonio Santos Villarreal. On the Mass Distribution and Birth Masses of Neutron Stars. , 757(1):55, September 2012. 1.2.1

[15] Aaron Smith. Tolman–oppenheimer–volkoff (tov) stars, 2012. 1.2.2

[16] Kohsuke Sumiyoshi, Toru Kojo, and Shun Furusawa. *Equation of State in Neutron Stars and Supernovae*, page 1–51. Springer Nature Singapore, 2023. 1.2.3

[17] Faber, J.A., Rasio, F.A. Binary Neutron Star Mergers. Living Rev. Relativ. 15, 8 (2012). 1.2.4

[18] T. M. Tauris, M. Kramer, P. C. C. Freire, N. Wex, H.-T. Janka, N. Langer, Ph. Podsiadlowski, E. Bozzo, S. Chaty, M. U. Kruckow, E. P. J. van den Heuvel, J. Antoniadis, R. P. Breton, and D. J. Champion. Formation of double neutron star systems. *The Astrophysical Journal*, 846(2):170, September 2017. 1.2.4

[19] E.P.J. van den Heuvel. Evolution of x-ray binaries: Achievements and advances. *Advances in Space Research*, 38(12):2667–2672, 2006. Spectra and Timing of Compact X-ray Binaries. 1.2.4

[20] Estelle Asmodelle. Tests of general relativity: A review, 2017. 1.2.4

[21] R Abbott. Gwtc-3: Compact binary coalescences observed by ligo and virgo during the second part of the third observing run. *Phys. Rev. X*, 13:041039, Dec 2023. 1.2.4

[22] Christopher M. Hirata. Lecture xxvi: Kerr black holes: I. metric structure and regularity of particle orbits, 2012. 1.3.36

[23] Pierre Fleury. *Gravitation: From Newton to Einstein*. Springer International Publishing, 2019. 1.4, 1.2

[24] K. D. Kokkotas and J. Ruoff. Radial oscillations of relativistic stars. *Astronomy amp; Astrophysics*, 366(2):565–572, February 2001. 2.1.1

[25] Joanna Piotrowska, Jonah M. Miller, and Erik Schnetter. Spectral methods in the presence of discontinuities. *Journal of Computational Physics*, 390:527–547, August 2019. 2.2

[26] Palenzuela c (2020) introduction to numerical relativity. front. astron. space sci. 7:58. doi: 10.3389/fspas.2020.00058. 2.2

[27] P. Grandclément, S. Bonazzola, E. Gourgoulhon, and J.-A. Marck. A multidomain spectral method for scalar and vectorial poisson equations with noncompact sources. *Journal of Computational Physics*, 170(1):231–260, June 2001. 2.2, 2.2

[28] Eric Gourgoulhon. An introduction to polynomial interpolation, 2005. 2.2

[29] T Baumgarte. Numerical relativity and compact binaries. *Physics Reports*, 376(2), mar 2003. 2.3

[30] He Gao and Shun-Ke Ai. Relation between gravitational mass and baryonic mass for non-rotating and rapidly rotating neutron stars. *Frontiers of Physics*, 15(2):24603, 2020. 3

[31] Ryne J Beachley, Morgan Mistysyn, Joshua A Faber, Steven J Weinstein, and Nathaniel S Barlow. Accurate closed-form trajectories of light around a kerr black hole using asymptotic approximants. *Classical and Quantum Gravity*, 35(20):205009, October 2018. 4.1, 4.2